A Comparison of Mesoscale Pressure Features Observed with Smartphones and Conventional Observations

CALLIE MCNICHOLAS[a] AND CLIFFORD F. MASS[a]

[a] *Department of Atmospheric Sciences, University of Washington, Seattle, Washington*

(Manuscript received 8 October 2021, in final form 10 February 2022)

ABSTRACT: To examine the utility of smartphone pressure observations (SPOs), a climatology of mesoscale pressure features was developed to evaluate whether SPOs could better resolve mesoscale phenomena than existing surface pressure networks (MADIS). A comparison between MADIS and smartphone pressure analyses was performed by tracking and characterizing bandpass-filtered, mesoscale pressure features. Over the year 2018, nearly 3000 pressure features were tracked across the central and eastern United States. Pressure features identified by smartphone observations lasted, on average, 25 min longer, traveled 25 km farther, and exhibited larger amplitudes than features observed by MADIS. An examination of smartphone pressure features tracks by season and location found that almost all pressure features propagated eastward. With over 87% of observed pressure features associated with convection, the climatology of surface pressure features largely reflects the geographic and seasonal variation of mesoscale convection. Phase relationships between pressure features and other surface variables were consistent with those expected for mesohighs and wake lows. These results suggest that SPOs could enhance convective analyses and forecasts compared to existing surface networks like MADIS by better resolving mesoscale structures and features, such as wake lows and mesohighs.

SIGNIFICANCE STATEMENT: While smartphone pressure networks provide unprecedented observation coverage and density, it was unclear whether they can add value to existing surface pressure networks. This study addresses this question by developing a yearlong record of mesoscale pressure features over the eastern and central United States. Analysis of this record revealed that smartphone analyses better resolved mesoscale pressure features, especially across the central United States where existing surface pressure networks are sparser. Nearly all observed pressure features were observed near precipitation, with five in six associated with convection. Relationships between mesoscale pressure features and other surface state variables were consistent with those expected for mesohighs and wake lows.

KEYWORDS: Convective storms/systems; Mesoscale systems; Squall lines; Climatology; Surface pressure; Data processing/distribution; In situ atmospheric observations; Surface observations; Filtering techniques; Statistical techniques; Seasonal variability

1. Introduction

Measurements of atmospheric pressure remain an essential tool for the detection, analysis, and prediction of atmospheric phenomena across spatial and temporal scales. Since atmospheric pressure reflects the three-dimensional structure of the atmosphere and is less prone to errors of representativeness than other surface variables (Madaus et al. 2014), surface pressure measurements have proved useful for the identification and tracking of mesoscale phenomena, even when other surface variables remain unperturbed (Jacques et al. 2017).

Surface pressure perturbations have been linked to a variety of phenomena, such as high-frequency internal gravity waves associated with deep convective diabatic heating (Adams-Selin and Johnson 2013), katabatic drainage flows (Viana et al. 2010), and inertia–gravity waves generated by topographic forcing, fronts, and geostrophic adjustment (Hooke and Jones 1986; Fritts and Alexander 2003; Kim et al. 2003; Koppel et al. 2000; Jewett et al. 2003). Fronts and drylines associated with midlatitude cyclones, differential heating of land–water surfaces, and atmospheric tides also generate surface pressure perturbations (Mass et al. 1991; Crawford and Bluestein 1997; Novak and Colle 2006; Gaberšek and Durran 2006; Geerts et al. 2008; Li et al. 2009; Li and Smith 2010; Pedatella et al. 2012; Giovannini et al. 2017; Price et al. 2018). Such pressure perturbations can also be produced by convection (Koch and Golus 1988; Metz and Bosart 2010; Adams-Selin and Johnson 2010). Convectively generated mesohighs and wake lows are often accompanied by strong winds (Fujita 1955; Johnson and Hamilton 1988; Evans and Doswell 2001; Engerer et al. 2008).

Only a handful of studies have produced climatologies of surface mesoscale pressure features. Koppel et al. (2000) created a climatology of large surface pressure fluctuations (>4.25 hPa) over 25 years. Their analysis was limited to large amplitude inertia–gravity waves due to their reliance on a sparse, hourly network of surface airways observations. de Groot-Hedlin et al. (2017) provided a multiyear climatology of near-surface gravity waves over the central and eastern United States by tracking mesoscale pressure perturbations from the subsynoptic Earthscope USArray Transportable Array (USArray) pressure network (Jacques et al. 2017; Tytell et al. 2016). The USArray pressure network, utilized by de Groot-Hedlin et al. (2017) to study gravity waves, has also been applied to examine the broader spatial and temporal characteristics of surface pressure perturbations. Jacques et al. (2015) decomposed two years of USArray surface pressure observations into

Corresponding author: Callie McNicholas, cmcnich@uw.edu

DOI: 10.1175/WAF-D-21-0166.1

mesoscale (10 min–4 h), subsynoptic (4–30 h), and synoptic (30–120 h) perturbations using a bandpass-filter approach (Koch and O'Handley 1997; Koch and Saleeby 2001). The spatial distribution of subsynoptic perturbations varied by season due to the diverse mechanisms responsible for their generation [e.g., fronts, mesoscale convective systems (MCS)]. For example, large magnitude mesoscale pressure perturbations were observed over the southern and central Great Plains during the spring and summer, respectively. Synoptic-scale pressure perturbations were strongest during the winter and exhibited a frequency and intensity maxima over the northeastern United States.

In a follow-up study, Jacques et al. (2017) tracked and cataloged mesoscale pressure perturbations over the central United States from 1 March to 31 August 2011. Using a 2D variational assimilation system (Tyndall and Horel 2013), 5-min 5-km pressure analyses were created by assimilating pressure tendency from bandpass-filtered USArray observation onto temporally interpolated pressure analyses from the real-time mesoscale analysis (RTMA; de Pondeca et al. 2011). Most mesoscale pressure features propagated over short distances (<200 km), were short-lived (<3 h), and were limited in areal extent (<40 000 km^2). Approximately, three in four features exhibited phase speeds of 15–35 m s^{-1}. Like the de Groot-Hedlin et al. (2017) study, the deployment strategy of the USArray network limited the temporal period and scale of the phenomena examined to >1 h and >10 000 km^2, respectively. Since the USArray network spanned only 10° of longitude, the duration and distance traveled of zonally propagating pressure features were likely underestimated. Jacques et al. (2017) examined large-amplitude surface pressure perturbations (>3 hPa), differentiating surface pressure features related to convection as either associated with an MCS or another type of "convective" feature. In total, 84% of all mesoscale pressure features exceeding 3 hPa in magnitude were associated with convection.

Previous climatologies of surface pressure features associated with mesoscale phenomena have been limited by a lack of density, temporal frequency (Koppel et al. 2000), and spatial extent of surface pressure observations (Jacques et al. 2015). To address this issue, the present study applies a network of surface pressure observations from smartphones of unprecedented density and spatial extent (McNicholas and Mass 2021). In McNicholas and Mass (2021), the bias correction, quality control (QC), and objective analysis of smartphone pressure observations were demonstrated. This paper extends this analysis to other surface state variables using MADIS data to facilitate a yearlong analysis of surface pressure features across the central and eastern United States. Expanding upon the work of Jacques et al. (2017), mesoscale pressure perturbations were extracted from MADIS and smartphone pressure analysis through bandpass filtering (Koch and O'Handley 1997). Using particle tracking at 5-min intervals (Allan et al. 2014) to identify features, climatologies of surface pressure features were produced. These climatologies, in combination with surface perturbations of other state variables, were employed to answer the following questions:

1) Do smartphone pressure analyses capture mesoscale pressure features poorly observed by existing surface pressure networks (e.g., MADIS).
2) How does the climatology of surface pressure features based on smartphone pressure observation vary geographically, seasonally, and diurnally? How do the results compare with prior research (e.g., Jacques et al. 2015; Jacques et al. 2017)?
3) What phase relationships exist between mesoscale pressure perturbations and other surface state variables? How do pressure perturbations relate to precipitation?

2. Observation datasets

Two datasets were used in this study and are described below. The first is a smartphone pressure dataset from The Weather Company (IBM), while the second includes pressure, temperature, moisture, and winds from conventional surface observations, provided by the Meteorological Assimilation Data Ingest System (MADIS; Miller et al. 2005). Observations from both datasets were retrieved from 15 August 2017 to 30 December 2018 across the central and eastern United States. The western United States was excluded due to the relative sparsity of MADIS and smartphone observations across the Intermountain West.

a. *MADIS observations*

MADIS includes observations from local mesonets (mesoscale observing networks) and METARs (Meteorological Aerodrome Reports) and applies three levels of QC checks. The majority of MADIS mesonet observations were provided by the Citizen Weather Observer Program (CWOP; www.wxqa.com), a network of personal weather stations (PWSs) maintained by private citizens. Mesonet observations report pressure to 0.01 hPa while METARs, provided by MADIS, report pressure to the nearest 0.01 in. of mercury (~0.33 hPa). To address the lower resolution of MADIS pressure observation at METAR location, 1-min station pressure observations with a resolution of ~0.03 hPa were retrieved from the Automated Surface Observing System (ASOS) archive (NCEI 2018). Following Eq. (2) of McNicholas and Mass (2018a), a 5-min station pressure average was computed and reduced to sea level assuming the *U.S. Standard Atmosphere, 1976* (COESA 1976).

All MADIS surface observations undergo up to three levels of QC. A validity check evaluates whether observations fell within a physically reasonable range (MADIS 2017). For temporal consistency, the rate of change of each surface variable is calculated to determine if a reasonable threshold was exceeded. Last, a spatial consistency (buddy) check compares surface observations to neighboring observations through optimum interpolation and cross validation (Miller et al. 2005). Since METAR observations from the ASOS archive were not quality controlled, the MADIS spatial consistency check was applied to these observations. On average, less than 1% of ASOS pressure observations were flagged by this QC check.

Following McNicholas and Mass (2021), the R package LatticeKrig (Nychka et al. 2016) was used to perform multiresolution kriging (Nychka et al. 2015) of MADIS pressure, surface

air temperature, surface dewpoint temperature, and near-surface wind component observations. Terrain elevation from the High-Resolution Rapid Refresh (HRRR; Alexander et al. 2017; Blaylock et al. 2017) was regridded and used as a linear covariate, as were temperature, dewpoint temperature, and wind component, infrared satellite brightness temperature, distance from coastline, and surface type (i.e., land/water). For temperature and dewpoint temperature, HRRR vegetation type and surface roughness were also used as linear covariates, allowed kriging analyses to depict realistic variations in temperature and wind in the presence of complex terrain and land-sea boundaries.

MADIS temperature, dewpoint temperature, and wind component analyses, with a spatial resolution of 0.05° (~5 km), were generated every 5 min between 15 August 2017 and 30 December 2018. The analysis domain covered most of the central and eastern United States, (28.5°–48.5°N, 105.5°–70.5°W). A total of 30 conditional simulations were performed with Lattice Krig to estimate analysis uncertainty. Kriging standard error was computed by calculating the standard deviation of the analysis variable for conditional simulations. This standard error was used to define uncertainty in Kalman temporal smoothing with a Rauch–Tung–Striebel (RTS) smoother, which was applied to time series of MADIS surface analyses at each grid point in the analysis domain. Following McNicholas and Mass (2021), RTS smoothing was performed over a series of 2-h time windows with a 1-h time step between windows.

b. *Smartphone pressure dataset*

All SPOs used in this study were provided by IBM and were retrieved from smartphones with unique identifiers (UIDs) through the Weather Channel (WC) app. For each SPO, sea level pressure was calculated using the DEM ground elevation following the approach of McNicholas and Mass (2018, 2021). SPO errors were estimated by binning SPOs into 5-min windows and bilinearly interpolating 5-min MADIS pressure analyses to the location of each SPO. Following McNicholas and Mass (2021), SPOs were bias-corrected, each month, using SPO error predictions from DBSCAN (Ester et al. 1996) and extreme gradient boosting (XGB; Chen and Guestrin 2016) models trained on data from all prior months. Historical biases, used in training, were calculated by subtracting observed pressures (from interpolated MADIS analyses) from SPOs. After bias correction, a gross spatial check (Madaus and Mass 2017) and a spatial consistency check (Miller and Benjamin 1992) were applied to remove SPOs in substantial disagreement with surrounding observations (McNicholas and Mass 2021). Bias corrected and QC'd SPOs were subsequently superobbed at a resolution of 5 km. These superobservations (superobs) were produced by calculating a weighted average of UID SPOs within a 5-km radius (McNicholas and Mass 2021).

TABLE 1. List of parameters used to initialize LatticeKrig multiresolution pressure analyses.

Parameter	Description	Value
NC	No. of lattice points in first level and along the largest dimension	75
nlevels	No. of levels for the multiresolution basis	2
a.wght	The weight given to the central lattice point in the spatial autoregression	4.5
lambda	Smoothing parameter (noise to signal ratio)	0.5
alpha	Relative variances for the multiresolution levels	0.1, 0.9

After bias correction and QC, superobbed SPOs were used to generate smartphone pressure analyses. These analyses were generated using the same multiresolution kriging and Kalman temporal smoothing employed to create MADIS pressure analyses. LatticeKrig parameters (Table 1) were unchanged and smartphone pressure analyses were produced at the same spatial and temporal resolution as MADIS pressure analyses. Smartphone pressure analyses were generated every 5 min between 1 January 2018 and 30 December 2018. These analyses were produced for the same domain as MADIS pressure analyses.

c. *Observation counts*

Table 2 lists the average 5-min observation count for surface variables, retrieved during April 2018 across the full analysis domain. Among MADIS surface variables, wind observations were most numerous followed by dewpoint, temperature, and pressure observations. MADIS reported fewer pressure observations overall as some MADIS providers (e.g., state DOTs) typically report only temperature and wind measurements. The 5-min SPOs, superobbed at 5-km resolution, outnumbered MADIS pressure observations by a ratio of 4:1.

3. Methodology

a. *Mesoscale perturbation analysis*

To extract and identify pressure perturbations associated with mesoscale weather phenomena, a frequency filtering approach was employed. This technique was applied to the kriging analysis of smartphone and MADIS altimeter observations for 2018 (McNicholas and Mass 2021). The resulting mesoscale perturbation analyses were used to identify and characterize mesoscale pressure features associated with sensible weather. In the following section, the method of identifying, tracking, and analyzing mesoscale pressure features is outlined. One case, featuring a long-lived prefrontal squall line, is examined to illustrate this methodology.

TABLE 2. Total count of observations (Ob), by type and provider, during the 5-min analysis window centered at 0045 UTC 4 Apr 2018. Note that these observation counts are valid for the entire analysis domain that spanned 20° of latitude (28.5°–48.5°N) and 40° of longitude (105.5°–70.5°W).

	Smartphone pressure (superobbed)	MADIS pressure	MADIS temperature	MADIS dewpoint	MADIS wind
5-min Ob count	20 798	5100	6867	6883	7525

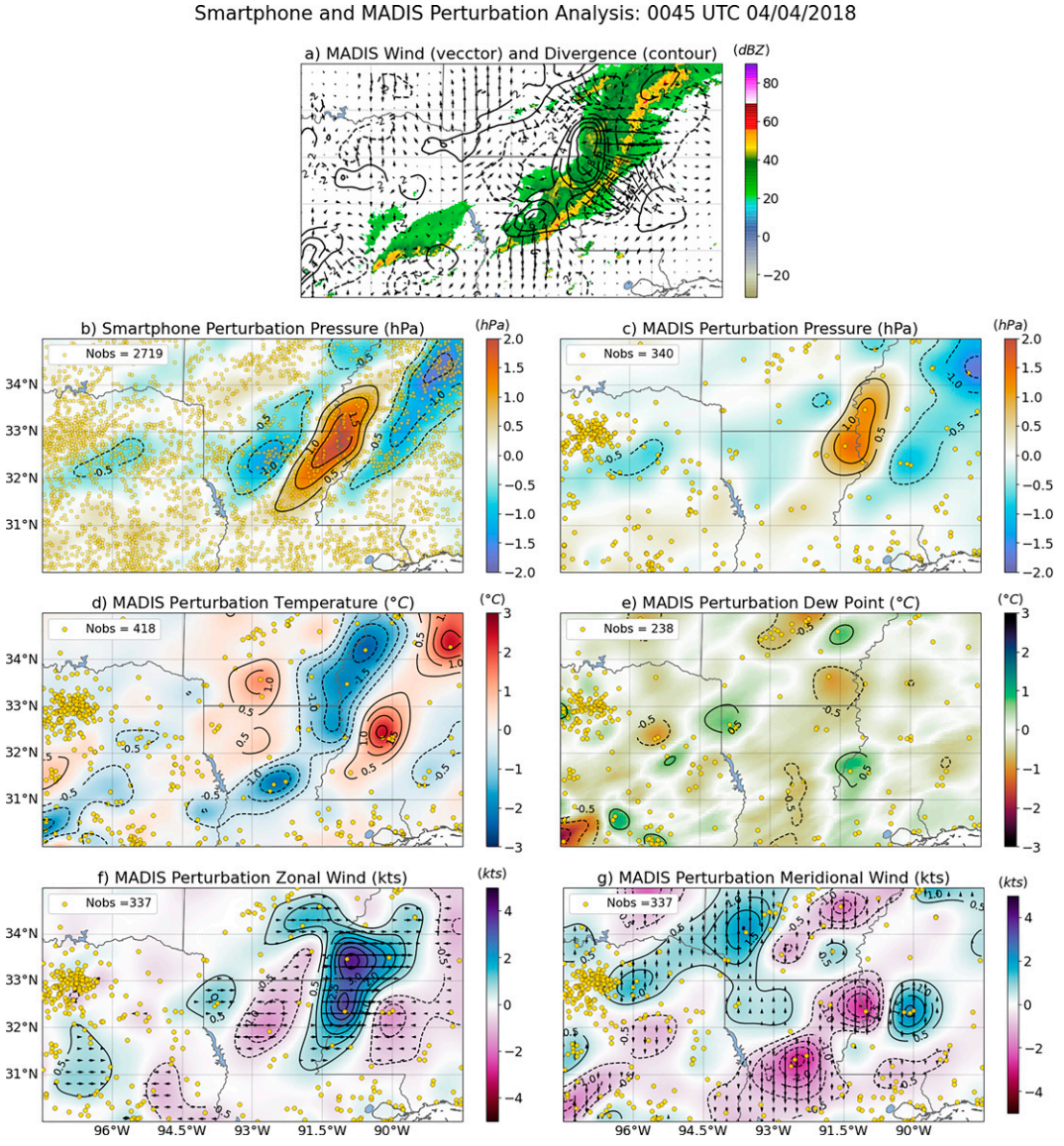

FIG. 1. The 2–6-h bandpass-filtered surface perturbation analyses of (b) smartphone pressure, (c) MADIS pressure, (d) MADIS temperature, (e) MADIS dewpoint temperature, and MADIS (f) zonal and (g) meridional winds for (a) a squall-line case at 0045 UTC 4 Apr 2018. In (a), smartphone pressure perturbations are overlaid on composite reflectivity. The location of observations used to generate multiresolution kriging analyses is shown as yellow markers.

To extract mesoscale pressure perturbations, a 2–6-h (fifth-order) bandpass filter was applied each month to time series at each point from MADIS and smartphone pressure analyses. Gaps in time series were filled by temporal interpolation if less than 12 h of data were missing during a month. To account for edge effects, time series from each month were extended to include data from the last day of the previous month and the first day of the following month. This frequency filtering approach was extended to other surface state variables to retrieve mesoscale temperature, dewpoint temperature, and wind component perturbations from MADIS analyses.

A visualization illustrating a surface perturbation analysis is provided in Fig. 1 for a squall-line case from April 2018. Mesoscale pressure perturbations associated with the squall line were larger in amplitude and spatial extent (Fig. 1b) in the smartphone analysis, relative to the MADIS analysis (Fig. 1c). Furthermore, the smartphone perturbation analysis captured a wake low that was poorly observed by MADIS due

TABLE 3. Trackpy parameters used to identify pressure features from monthly mesoscale pressure perturbation analyses.

TrackPy parameter	Parameter value
search_range	5 grid points (25 km)
Memory	2 frames (10 min)
Threshold	12 frames (1 h)

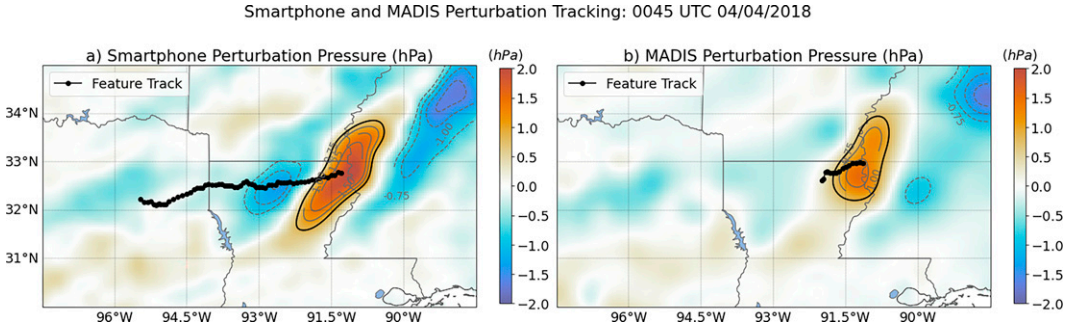

FIG. 2. Track of a positive mesoscale pressure perturbation associated with a squall line, observed in both (a) smartphone and (b) MADIS perturbation analysis. Black dotted lines depict the past locations of the feature centroid. The solid black contour highlights the feature (i.e., where $p' > 0.75$ hPa).

to a lack of observation density (Figs. 1b,c). The MADIS temperature perturbation analysis revealed positive temperature perturbations preceding the squall line and large negative temperature perturbations in the region of stratiform precipitation behind the convective line (Fig. 1d). Similarly, wind observations from MADIS captured zonal and meridional wind perturbations (Figs. 1f,g) that revealed convergence ahead of the squall line and divergence in its wake (Fig. 1a).

b. Feature identification and tracking

In this study, mesoscale pressure features were defined based on several spatial and temporal criteria. Pressure perturbations, like those shown in Figs. 1b and 1c, were masked (selected) where the value of the perturbation field exceeded ±0.75 hPa.[1] Masked objects were removed if no grid point within the masked area exceeded ±1 hPa. The centroids of masked objects were tracked with the Python TrackPy package (Allan et al. 2014) at 5-min intervals. TrackPy parameters are listed in Table 3. Object centroids were allowed to move up to five grid points (25 km) between frames. Objects that disappeared and reappeared within two frames (10 min) were considered identical. To be considered a feature, the object had to be tracked for a minimum of twelve frames (1 h). Last, a spatial filter was applied to remove feature objects if their maximum areal extent never exceeded 2500 km^2. This filter was applied to eliminate small spurious pressure features, many of which were too small to be characterized using surface analyses derived from MADIS observations, which have an average station separation of ~25 km (McNicholas and Mass 2021). Feature objects near the edge of the analysis domain, whose start/endpoint was within 1° of the grid boundary, were removed. Pressure features insufficiently resolved by the MADIS surface network were removed. Specifically, features whose contoured area passed over fewer than five MADIS surface temperature/wind observations over their lifetime were removed.

An example of mesoscale pressure object tracking is provided in Fig. 2, which shows the track path and object centroid for a positive pressure feature associated with the squall line depicted in Fig. 1. On the left, a smartphone pressure feature track extends from east Texas to the Louisiana–Mississippi border. The final point in the track marks the centroid of the smartphone pressure feature at the time of the analysis. In contrast, the plot on the right shows the track of a MADIS pressure feature, whose duration and extent was notably less than the smartphone pressure feature on the left.

c. Composite and cross-spectral analysis

To evaluate the structure and evolution of mesoscale pressure features, a compositing technique was developed. This approach, depicted in Fig. 3, involves extracting 12-h time series at grid points within a 250 km × 250 km bounding box centered at each time step (i.e., 5-min frame). As illustrated in the left panel of Fig. 3, the bounding box follows the centroid of the mesoscale pressure feature as it propagates across the domain. For each time, 2500 time series are extracted from grid points within the box (Fig. 3, right panel), producing a four-dimensional time-lagged ensemble of perturbation time series. Composite analyses were generated by averaging these time series, resulting in three-dimensional analyses represent the composite spatiotemporal evolution of the pressure feature along its track. Figure 4 illustrates the composite analyses for the smartphone pressure feature tracked in Fig. 3 and depicts the changing morphology of the pressure feature.

While TrackPy provides the estimated positions of the feature centroids, these location estimates are sensitive to changes in feature morphology, which is defined by a single contour line (±0.75 hPa). To estimate the velocity of mesoscale pressure features a beamsteering approach was employed (described in the appendix). Figure 5 shows the direction of feature propagation, derived through beamsteering, for the squall-line case. For the squall-line feature, the estimated phase speed was 17.5 m s^{-1} [see Eq. (A4)]. Once the direction of propagation is determined, the perturbation wind component parallel to the direction of feature propagation is calculated as follows:

$$U^{*\prime} = -u' \sin\alpha - v' \cos\alpha, \tag{1}$$

[1] This threshold was selected since the root-mean-squared error of smartphone pressure analyses in 2018 peaked at 0.75 hPa (McNicholas and Mass 2021).

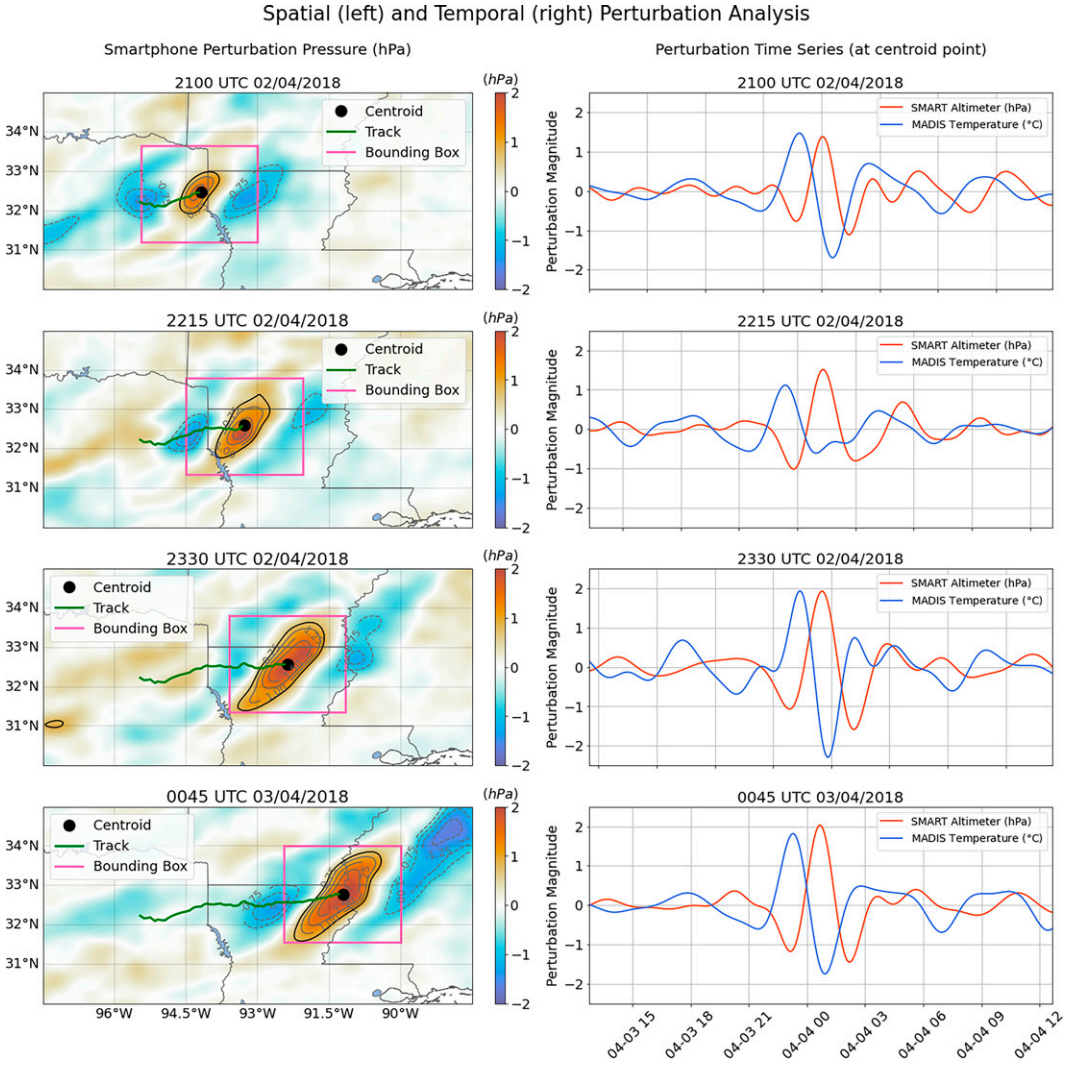

FIG. 3. (left) Spatial and (right) temporal analysis of the positive smartphone pressure feature from the squall-line case. In the left column, the positive mesoscale pressure feature is tracked (green line) and followed by a bounding box (pink) encompassing the area in which perturbation time series are extracted for compositing. In the right column, time series of smartphone pressure and MADIS temperature perturbations retrieved at feature centroid points (black dots) are displayed.

where u' and v' are cartesian perturbation wind components and α is the direction from which the feature is propagating. Figure 5b shows the results of this calculation for the composite pressure feature tracked in Fig. 4. Analysis of the feature normal wind perturbation $U^{*\prime}$ suggests a close phase relationship between pressure and wind, with wind perturbations preceding pressure perturbations of the same sign.

For a more quantitative evaluation of the phase relationships between mesoscale pressure features and surface state variables, cross-spectral analysis was employed. An example of this analysis is provided in Fig. 6, which shows the cross-spectral analysis of composite pressure and feature normal wind time series, retrieved at the center of the composite analysis grid. The cross-spectral density (CSD) of pressure and feature normal wind perturbations is shown in Fig. 6b, with a dashed line indicating the frequency of the maximum CSD derived from beamsteering analysis (Fig. A1). At this frequency (~0.004 min^{-1}), the coherence between pressure and feature normal wind was 0.97 (Fig. 7c). The phase angle between feature normal wind and pressure perturbations was approximately 36° (Fig. 6d). This phase relationship is consistent with the solitary model of deep convection (Fujita 1955; Koch and Golus 1988), wherein surface wind perturbations precede pressure perturbations of the same sign.

4. Results

a. *Smartphone and MADIS comparison*

A key question is whether SPOs and analyses based on them can detect and resolve mesoscale meteorological phenomena

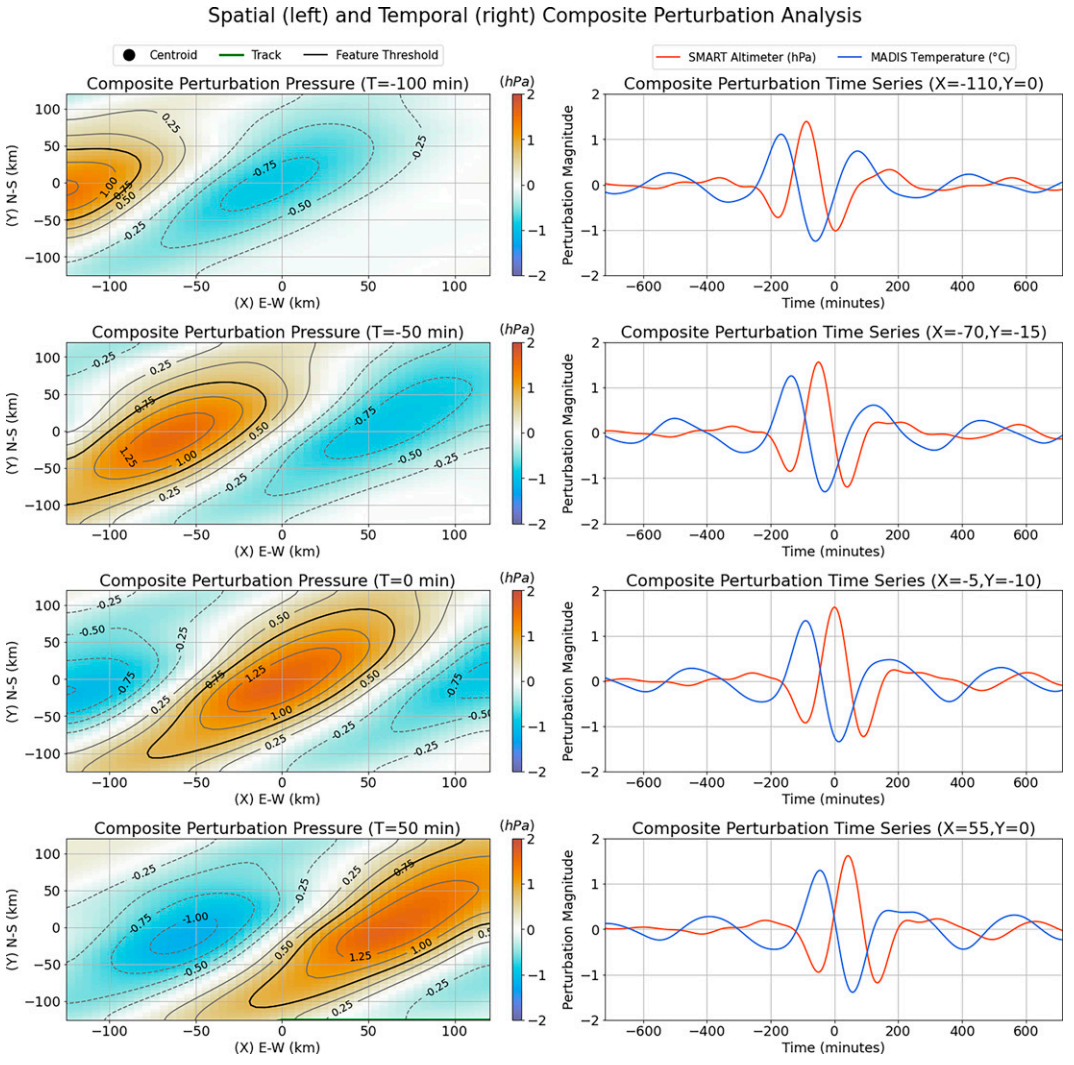

FIG. 4. (left) Spatial and (right) temporal composite analysis of the positive smartphone pressure feature from the squall-line case. In the left column, the composite mesoscale pressure feature is tracked (green) in space. Composite time series, extracted at the centroid of the composite feature (black dots), are displayed in the right column.

better than existing surface pressure networks such as MADIS. To answer this question, MADIS and smartphone pressure feature climatologies were compared.

Throughout 2018, a total of 2897 smartphone pressure features and 2790 MADIS pressure features were detected (Table 4). Approximately 52% (51%) of smartphone (MADIS) features were associated with negative pressure perturbations. The similarity in feature counts between positive and negative features is sensible given the conservation of mass. Almost all MADIS and smartphone pressure features were observed within 50 km of precipitation, which is consistent with Jacques et al. (2017), who found that 97% of mesoscale pressure features were associated with precipitation. In this study, 86% of MADIS pressure features and 88% of smartphone pressure features were observed within 50 km of convection. While the percentage of features associated with precipitation was similar for both MADIS and smartphone climatologies, the magnitude of the features differed. Features with peak perturbations of at least double the perturbation threshold (0.75 hPa) were detected more frequently in the smartphone feature climatology (35%) than in the MADIS feature climatology (26%).

Smartphone and MADIS pressure feature tracks are plotted by sign in Fig. 7. In both climatologies, most features were detected in the western half of the domain. In all quadrants of the domain, smartphone feature counts exceeded MADIS feature counts (Figs. 7a,b). As in the total count (Table 4), slightly more negative features than positive features observed were also detected in all quadrants. In contrast to smartphone feature tracks, MADIS tracks were more tightly clustered due to the sparsity and irregular spacing of MADIS pressure observations (Fig. 7b). The clustering of MADIS feature tracks produced large gaps in feature track coverage where MADIS pressure observations were sparse (e.g., southeast Georgia).

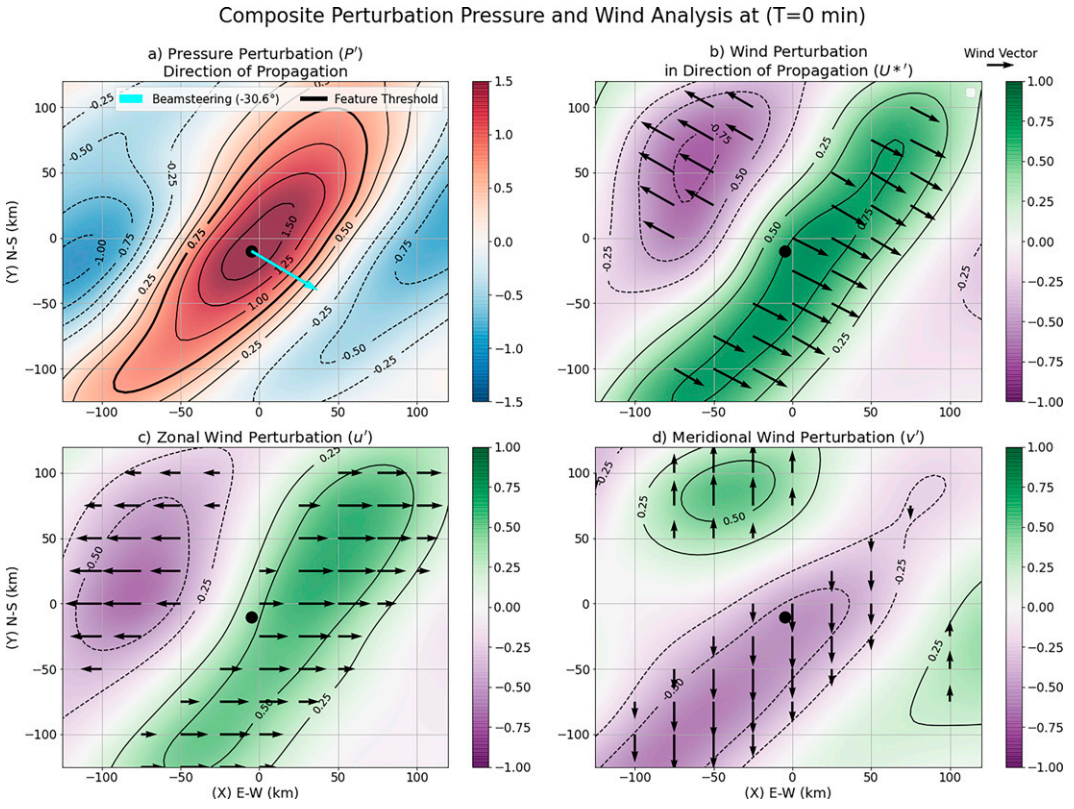

FIG. 5. (b) Feature normal wind, derived from (c),(d) perturbation wind components, and (a) the direction of feature propagation. The feature propagation direction, derived from cross-correlation lag-analysis and beamsteering, is indicated by colored arrows in (a). Composite perturbation wind and pressure analyses are displayed at $T = 0$ min.

Figure 8 displays the number of unique smartphone and MADIS features (i.e., perturbation events) for each 5-km horizontal grid cell within the domain. Local maxima in the number of pressure perturbations events appear in the southern and northern Great Plains (Fig. 8a), which is consistent with spring and summertime maxima in feature counts observed by Jacques et al. (2017). As in Fig. 7, most perturbation events occurred over the western half of the domain (Figs. 8a,b). In the eastern half of the domain, the difference between smartphone and MADIS pressure event counts was minimal, while in the western half of the domain, the average grid cell saw 7–10 more smartphone features than MADIS features. Thus, it appears MADIS observations lacked the spatial and temporal density over the Great Plains to capture pressure perturbations that could meet the detection threshold. One exception to this pattern is west Texas, where MADIS incorporates observations from the West Texas Mesonet.

A comparison of the characteristics of smartphone and MADIS pressure features is found in Fig. 9. Smartphone pressure features exhibited a larger average amplitude than MADIS pressure features (Fig. 9a) because the spatial and temporal density of SPOs was greater than MADIS pressure observations. While the amplitude of MADIS and smartphone pressure features differed, their maximum areal extent was similar (Fig. 9b), with the median pressure feature of each having a maximum area of around 40 000 km^2. In Jacques et al. (2017) most pressure features had a small areal extent (<40 000 km^2). This difference is likely attributed to the fact that the maximum feature extent in Jacques et al. (2017) was limited by the size of the USArray network, which was confined to a region between 100° and 90°W, and limited period of study, which spanned from March to August 2011. In Jacques et al. (2017), most observed features lasted less than three hours and traveled less than 200 km. Analysis of smartphone and MADIS pressure features were similar in those characteristics. The median duration of smartphone and MADIS features was 120 and 95 min, respectively, and the average smartphone (MADIS) pressure feature traveled 105 (80) km. The difference in feature duration and distance traveled between MADIS and smartphone features is consistent with SPOs better resolving mesoscale pressure perturbations, allowing them to be tracked longer and farther.

b. *Seasonal feature analysis*

Although most pressure features examined in this study were associated with convection (Table 4), this association varied depending on the season and sign of the perturbation. Figure 10 highlights these differences by displaying the distribution of maximum neighborhood reflectivity (NREFL) for positive and negative features during each season. This statistic was calculated by

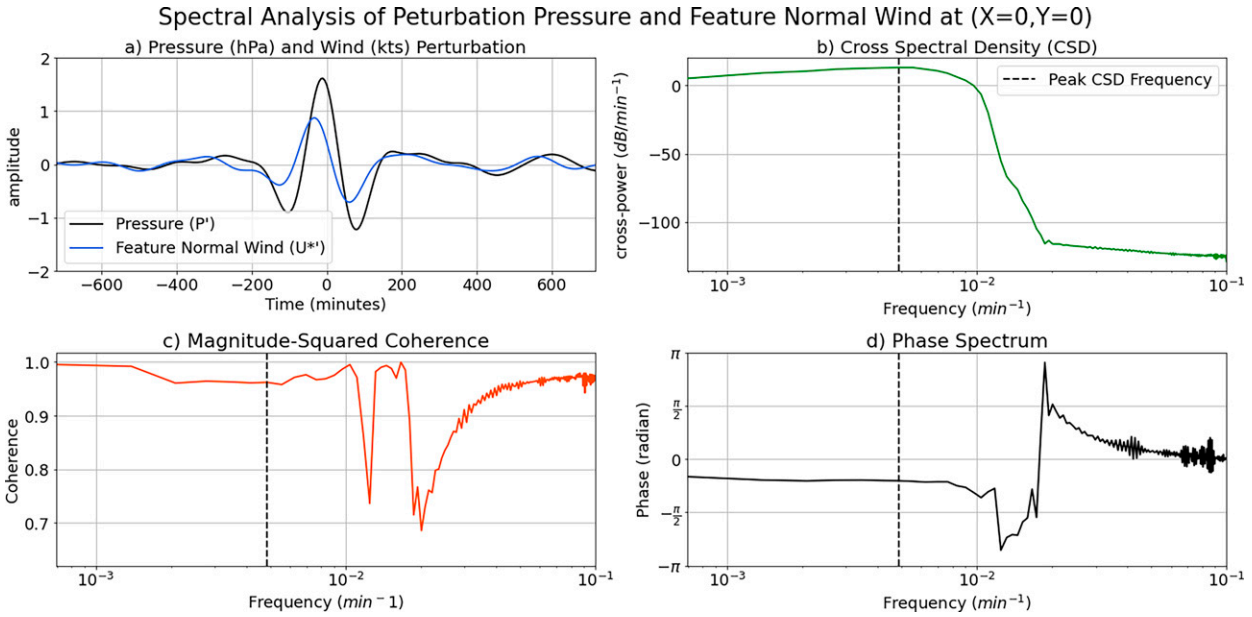

FIG. 6. (a)–(d) Cross-spectral analysis of pressure and feature-normal wind time series, extracted at the center of the composite domain. Cross-power spectral density (CSD) is displayed in (b), and magnitude squared coherence is displayed in (c). Phase is provided in (d). The dashed (vertical) line in (b)–(d) marks the frequency of the peak CSD, used to evaluate the coherence and phase of the feature.

retrieving the maximum value of composite reflectivity within 50 km of feature centroids. During all seasons, positive pressure perturbations were associated with higher values of NREFL than negative features. The difference in NREFL between positive and negative pressure features increased during the spring and summer months as the mode of precipitation evolved from stratiform to convective. Furthermore, the median NREFL for both positive and negative pressure features rose from ~45 dBZ during the winter to over 55 dBZ during the summer. During the summer, the median NREFL was ~60 dBZ for positive pressure features and 54 dBZ for negative pressure features, and the distribution of NREFL for positive pressure features became more concentrated around the mean (leptokurtic). This narrowed distribution may be attributed to squall line and MCS positive pressure perturbations during summer being dominated by the leading convective line where reflectivity values are highest (Johnson and Hamilton 1988). Conversely, wake lows are typically observed in the stratiform region behind the convective line and mesohigh (Coleman and Knupp 2009). This explains the gap in NREFL values between positive and negative pressure features during the summer month when over 92% of features were associated with mesoscale convection (>35 dBZ).

While smartphone and MADIS features exhibited similar total counts (Table 4), considerable variability in feature count was observed by month (Fig. 11). During the 1-yr period, both MADIS and smartphone pressure feature counts peaked between April and July (Figs. 11a,b). During the summer months, the difference in feature count between smartphone and MADIS increased (Fig. 11c), with more smartphone than MADIS pressure features detected between May and August. This difference may be attributed to the increase in organized mesoscale convection during the spring and summer months within the Great Plains (Haberlie and Ashley 2019) where MADIS pressure observations are sparser (McNicholas and Mass 2021).

Figure 12 displays the number of smartphone pressure features (perturbation events), that passed over each 5-km grid cell, by season. Although only available for a single calendar year (2018), the spatial distribution of pressure perturbation events by season largely agrees with prior work by Jacques et al. (2015), who observed a peak in mesoscale pressure events across the central Plains during the spring and summer months. During that half of the year, perturbation events were largely concentrated west of the Mississippi (Figs. 12b,c). In both spring and summer, local maxima in perturbation events were observed in the northern central plains where previous studies have found peaks in MCS (Haberlie and Ashley 2019) and AGW activity (DeGroot Hedlin et al. 2017). During the winter (Fig. 12a) and fall (Fig. 12d), there were fewer pressure perturbations across the domain since most pressure perturbation events are associated with convection (Table 4), whose incidence is typically reduced during that period.

Seasonal variation in both the spatial extent and magnitude of smartphone pressure features was observed. Figure 13 shows the distribution of smartphone feature magnitude for each season. On average, feature magnitudes were larger during the spring and summer, when the intensity of convection was greater (Fig. 10). In the fall, the landfalls of Hurricane Florence and Hurricane Michael were responsible for outliers in feature magnitude.

c. *Feature velocity and environment*

For each feature, the distance between feature centroids and the time between frames were used to estimate the average speed and direction of the pressure perturbation. The frequency distribution of smartphone feature perturbation velocity is

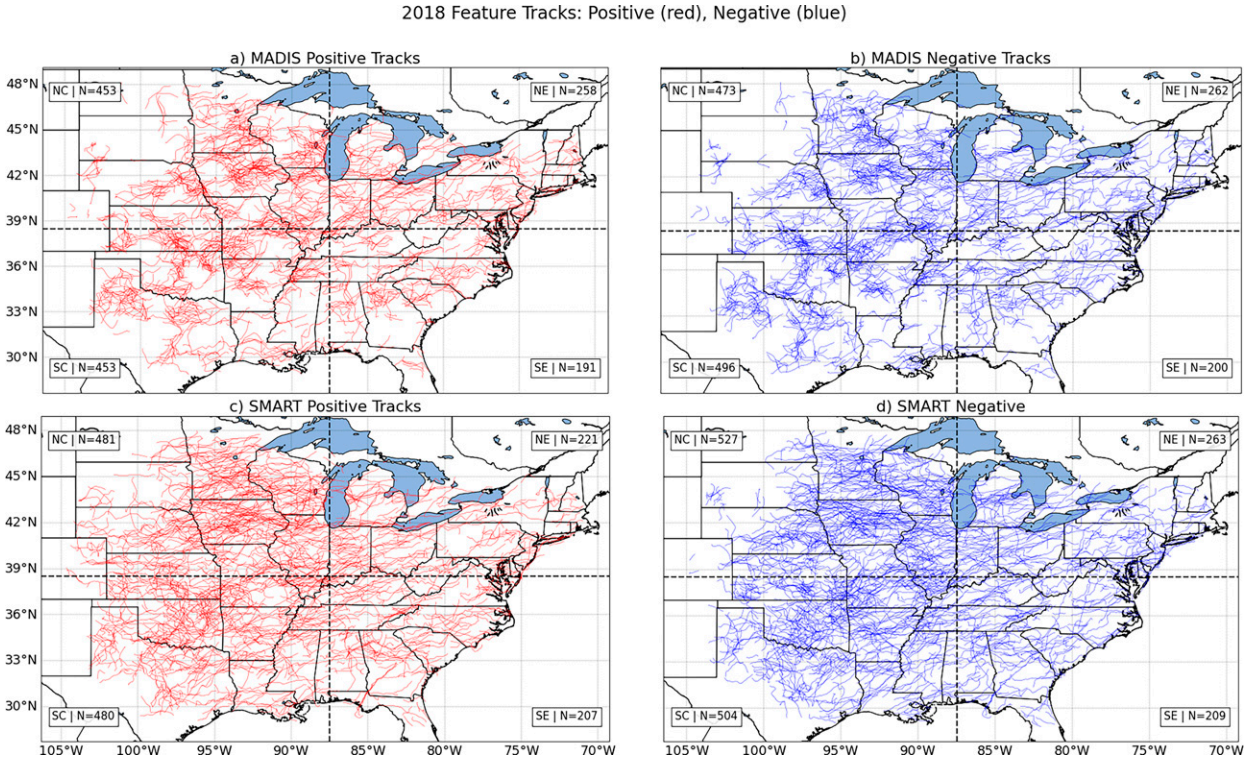

FIG. 7. (bottom) Smartphone and (top) MADIS feature tracks for positive (red) and negative (blue) perturbations from the year 2018. Feature counts for each geographic quadrant (NC: north-central, SC: south-central, NE: northeast, SE: southeast) are displayed in their respective corners.

displayed in Fig. 14. Across the full domain, the direction of feature perturbation propagation veered from northeastward during the winter to southeastward during the summer. On average, feature perturbations moved faster during the winter (~23 m s^{-1}) than during the summer (19 m s^{-1}) due to stronger synoptic forcing during that season, consistent with the results of Jacques et al. (2015). Between the winter and summer, the percentage of features propagating in a westerly direction rose from 3% to 8%. During all seasons, the mean perturbation speed of westward propagating features was considerably lower (~15 m s^{-1}) than eastward propagating features (~21 m s^{-1}).

Most of the pressure features analyzed in this study were associated with mesoscale convection, which is typically associated with a sinusoidal variation in perturbation pressure and wind (Vescio and Johnson 1992). This wave-like characteristic of convectively induced pressure perturbations motivated the estimation of pressure feature phase velocity through beamsteering (see the appendix). Note that the phase velocity is the velocity of the pressure wave associated with the feature while the perturbation velocity is the average velocity of the ±0.75 hPa perturbation contour which outlines the feature (Fig. 3). A comparison between the perturbation velocity and phase velocity is provided for smartphone pressure features in Fig. 15. On average, the feature phase speed (Fig. 15b) was greater than the feature perturbation speed (Fig. 15a) by approximately 7 m s^{-1}. This finding is consistent with Vescio and Johnson (1992) who observed that perturbation pressure waves associated with squall lines tend to propagate faster than air parcels within them.

While the preferred direction of propagation for perturbations (Fig. 15d) was eastward the direction of wave phase propagation was predominately southeastward (Fig. 15e). This difference in perturbation velocity and phase velocity is highlighted in Fig. 15f. For approximately 72% of smartphone pressure features the direction of phase propagation was veered (rotated clockwise) with respect to the direction of perturbation propagation. This result is reminiscent of Rees et al. (2000) who examined gravity

TABLE 4. Counts (percentages) of MADIS and smartphone pressure features by sign, magnitude, and proximity to precipitation. Features were associated with precipitation if composite reflectivity values exceeding 20 dBZ were detected within 50 km of a feature centroid.

Category	Feature count (%)
MADIS	2790 (100%)
Positive	1357 (49%)
Negative	1433 (51%)
Precipitation (dBZ > 20)	2667 (96%)
Convective precipitation (dBZ > 35)	2398 (86%)
Magnitude $\|p'\|$ > 1.5 hPa	733 (26%)
Smartphone	2897 (100%)
Positive	1390 (48%)
Negative	1507 (52%)
Precipitation (dBZ > 20)	2799 (97%)
Convective precipitation (dBZ > 35)	2536 (88%)
Magnitude $\|p'\|$ > 1.5 hPa	1022 (35%)

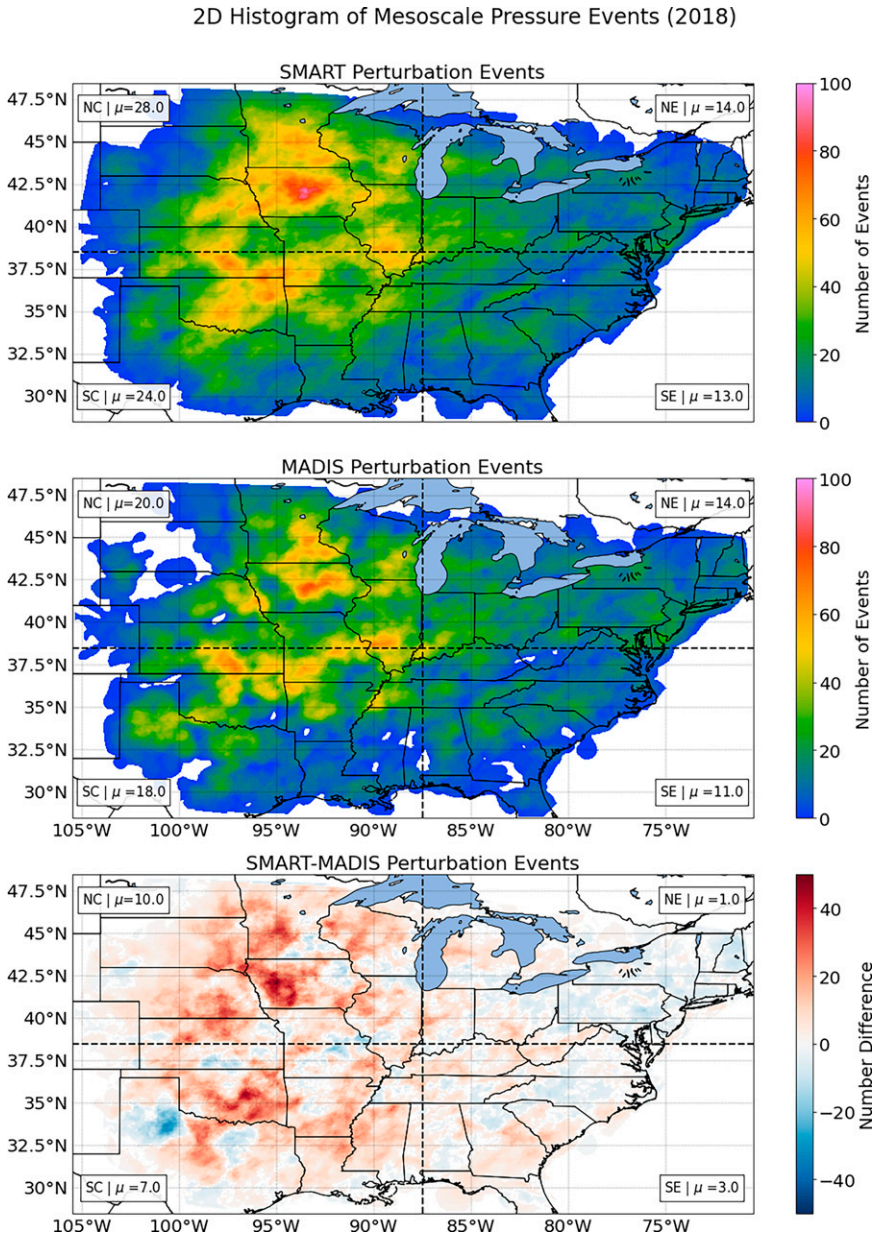

FIG. 8. Spatial histogram of perturbation events split into four geographic quadrants. Perturbation events were counted by the number of unique features that passed over a 5-km grid cell during the year 2018. The average event count for each quadrant is displayed in each corner.

waves with time series of pressure perturbations from Antarctica. In their analysis, they observed that, for most wave-like pressure perturbations, the direction of wave propagation veered from the mean wind. This implies that the phase lines of pressure waves associated with convection are typically not perpendicular to the mean wind.

d. Composite feature analysis

To examine the relationship between mesoscale pressure perturbations and other surface state variables, composite analyses of smartphone pressure features were performed following the methodology introduced in section 3, using MADIS observations for variables other than pressure. The distribution of composite time series, retrieved at the center of the composite domain (Fig. 4), is shown for all smartphone pressure features in Fig. 16.

In Fig. 16a, the distribution of composite time series of perturbation pressure is displayed for both positive and negative smartphone pressure features. In both time series, the primary perturbation is preceded and followed by a smaller perturbation of the opposite sign, indicative of the wave-like nature of observed mesoscale pressure perturbations (Fig. 16a). Composite

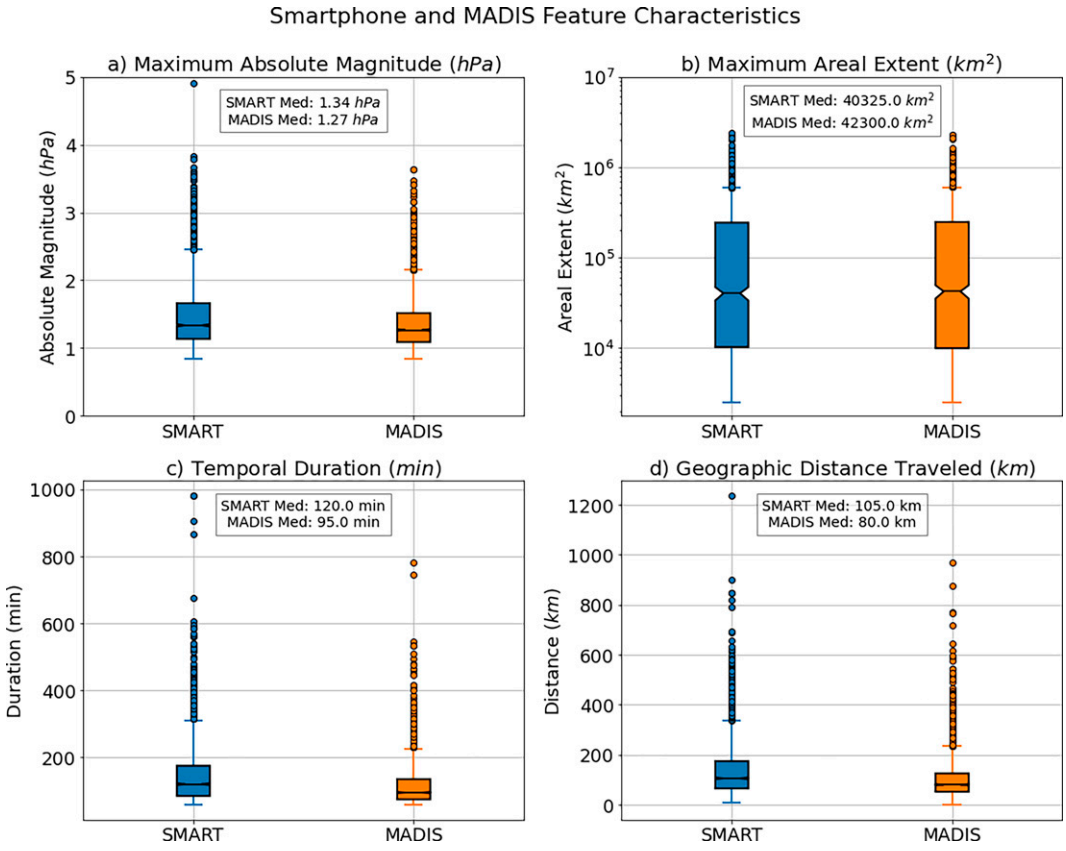

FIG. 9. Distribution of smartphone (blue) and MADIS (orange) feature characteristics. (a) The maximum absolute magnitude and (b) areal extent of feature perturbations. (c) Feature duration and (d) distance traveled. Median statistics for each characteristic are embedded in each plot.

time series of other surface state variables (Figs. 16b–d) indicate that the feature-normal wind field responded strongly to perturbations in pressure. On average, feature-normal wind perturbations slightly lead perturbation pressure, with peaks in wind perturbations (Fig. 16b) preceding corresponding peaks in perturbation pressure (Fig. 16a). Temperature and dewpoint temperature perturbations similarly lead perturbations in pressure but to a greater degree (Figs. 16c,d).

In general, positive (negative) pressure features were associated with positive (negative) normal wind perturbations, indicative of a positive correlation between pressure and wind perturbations. Conversely, temperature and dewpoint perturbations were negatively correlated with perturbation pressure as positive pressure perturbations were coincident with negative temperature/dewpoint perturbations. Interestingly, positive (negative) perturbations were associated with local maxima (minima) in reflectivity. Given that 97% of pressure features were observed in proximity to precipitation, this suggests that positive (negative) pressure perturbations were generally mesohighs (wake lows). This is further evidenced by the fact that composite time series of perturbation pressure and reflectivity are consistent with models of convective precipitation that place a mesohigh beneath a leading line of stronger precipitation (Fig. 17a) and a wake low to the lee of the mesohigh (Fig. 17b) in a region of lighter (stratiform) precipitation (Fig. 16).

In Fig. 18, spatial composite analyses, retrieved at the center of the compositing time window, were averaged separately for positive and negative smartphone pressure features. Overlaid on each plot, a vector field depicts the feature-normal wind perturbation field. The axis of mean composite perturbations was oriented southwest to northeast as the direction of phase propagation for most features was southeastward (Fig. 15e). For positive (negative) pressure perturbations (Fig. 18a), the perturbation wind field was divergent (convergent). On average, this line of divergence/convergence was displaced rearward of the pressure perturbation because the speed of the pressure wave typically exceeded the perturbation speed (Fig. 15).

This result is consistent with the findings of Vescio and Johnson (1992) who observed a similar phase shift between wave normal wind perturbations and pressure perturbations in squall lines, independent of wave amplitude. Ahead of the positive perturbation (mesohigh) and behind the negative perturbation (wake low) convergence was observed (Fig. 18b). Convergence behind the wake low appears in tandem with a local maximum in composite reflectivity, suggesting that convergence behind the wake low contributes to the development of new precipitation (Johnson and Hamilton 1988).

The dynamics of this spatial climatology presented in Fig. 18 can be explained by precipitation processes. Positive pressure

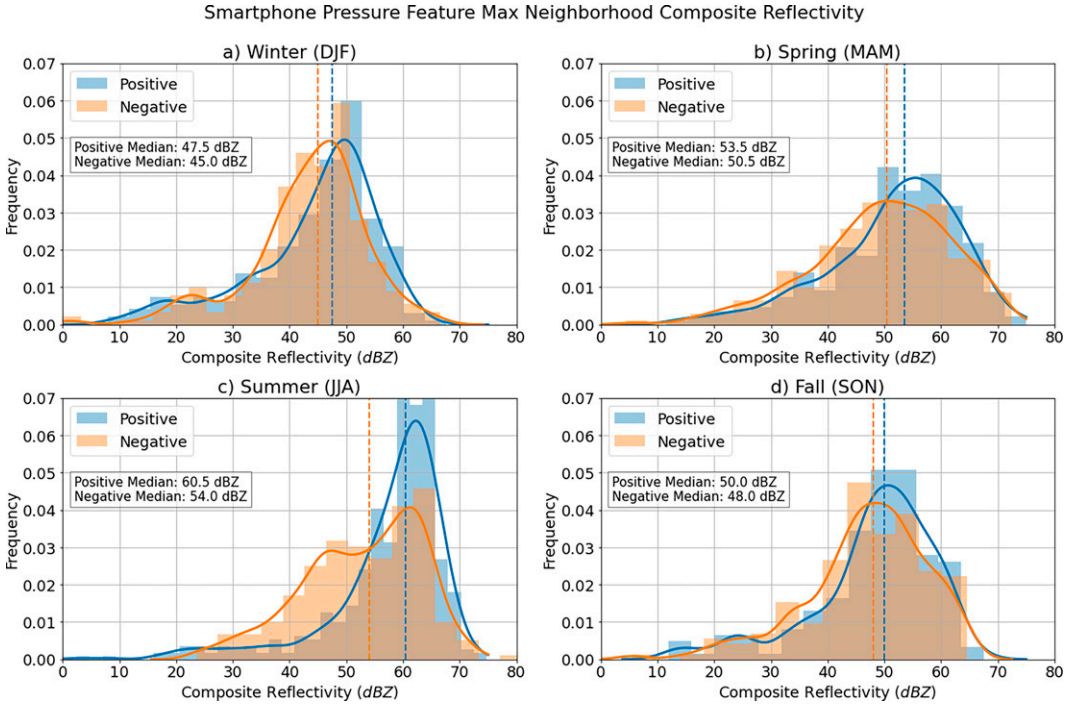

FIG. 10. Seasonal distribution of maximum neighborhood reflectivity for smartphone pressure features. Each frame the neighborhood reflectivity was assessed by calculating the peak value of composite reflectivity within 50 km of the feature centroid. The maximum value observed over the lifetime of each feature is shown above, for both positive (blue) and negative (orange) features. Probability density functions (PDFs), derived through kernel density estimation, are overlaid atop histograms of the same color.

perturbations (mesohighs), observed beneath more intense precipitation (Fig. 18e), are produced by evaporative cooling and hydrometeor loading in downdrafts (Haertel and Johnson 2000). This cooling is visible in average composite analyses of surface temperature and perturbations (Fig. 18c). Behind the mesohigh, a wake low is produced by adiabatic warming from subsidence (Fig. 17a; Coleman and Knupp 2009). Consequently, positive temperature perturbations are observed in the mean composite analysis of negative pressure features (Fig. 18c). On average, perturbations in dewpoint temperature were small and consistent in sign with observed temperature perturbations (Fig. 18d).

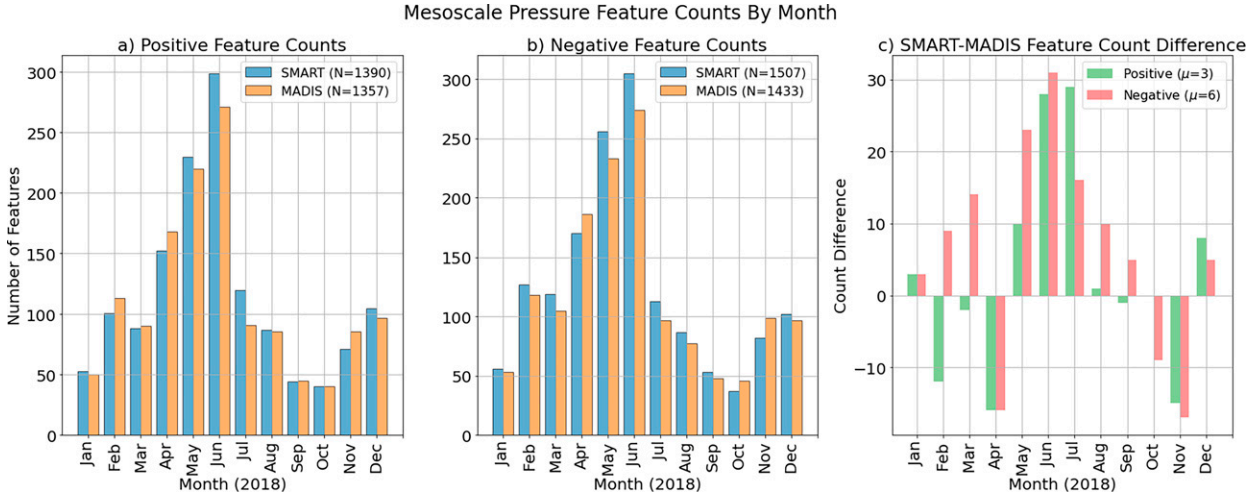

FIG. 11. Monthly feature counts for (a) positive and (b) negative smartphone and MADIS features. (c) The difference in monthly feature count between smartphone (SMART) and MADIS is displayed.

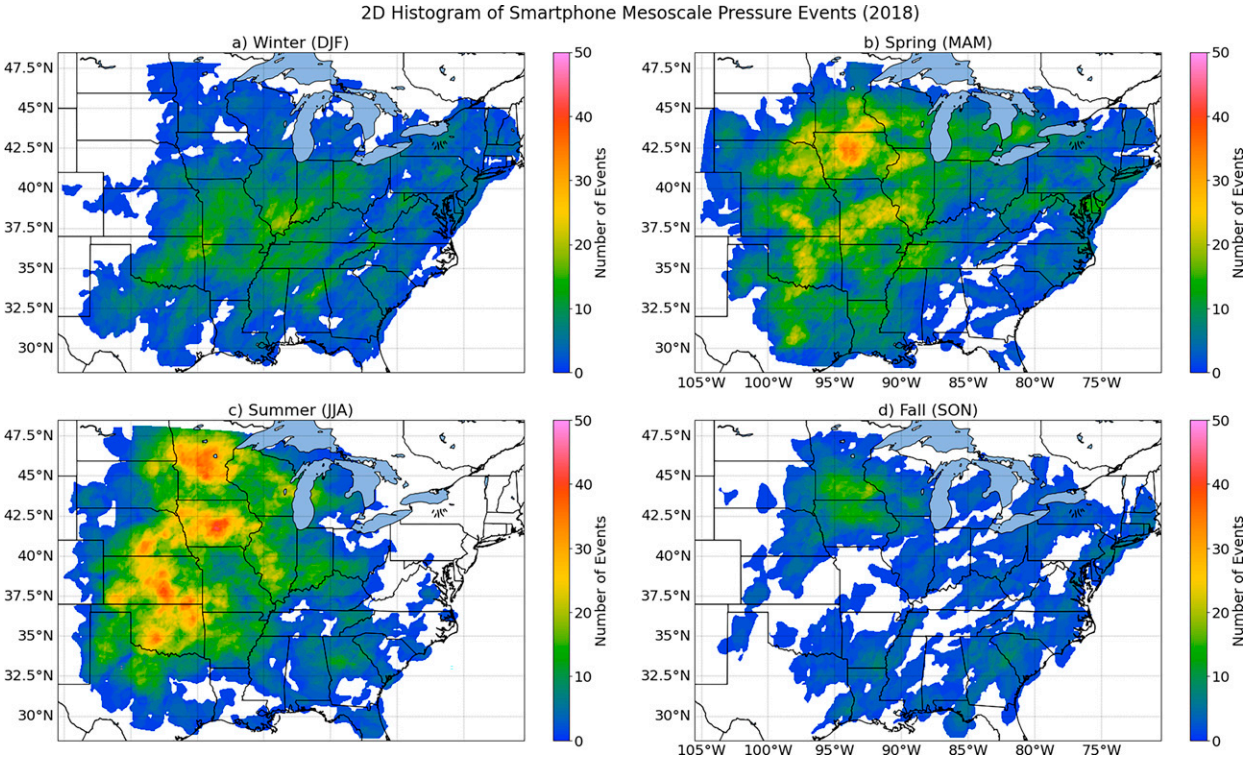

FIG. 12. Spatial histogram of perturbation events by season. Perturbation events were counted by the number of unique features that passed over a 5-km grid cell during the given season.

Averages of feature composites indicate that wind, temperature, and dewpoint perturbations usually lead perturbations in pressure (Fig. 18). In the analysis of composite time series, the correlation between wind and pressure perturbations appeared to be stronger than for pressure and temperature perturbations (Fig. 16). To further examine these subjective findings, a quantitative analysis of the phase and coherence of smartphone pressure features was performed. Figure 19 highlights the results of this analysis, for positive and negative pressure features, through 2D stacked histograms that show the distribution of phase and coherence between perturbation pressure and feature temperature, dewpoint, and normal wind perturbations.

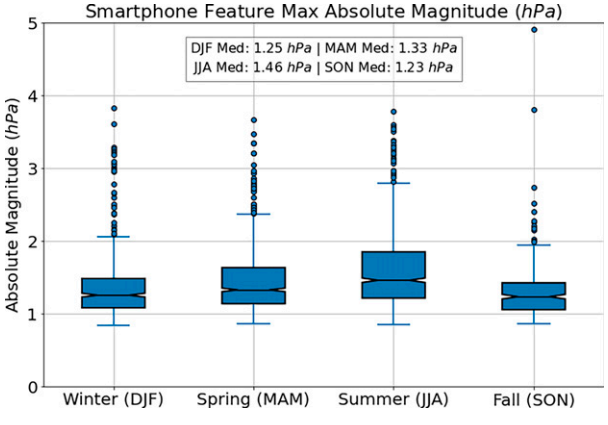

FIG. 13. Seasonal distribution of smartphone feature maximum absolute amplitude. This statistic was calculated as the absolute value of the maximum magnitude of the pressure perturbation over the lifetime of the feature. Boxes depict the interquartile range (IQR) of the distribution. Notches in each boxplot indicate bootstrapped confidence intervals for the median. The median feature maximum magnitude is displayed above the boxplots.

Phase and coherence relationships, between pressure and other surface state variables, were not sensitive to the sign of pressure perturbation (Fig. 19). For both negative and positive pressure features the average coherence between pressure and feature normal wind was high (~0.8). For temperature and dewpoint perturbations the average coherence with pressure was lower at 0.57 and 0.53, respectively. Concerning phase, the feature normal wind consistently leads perturbation pressure by a phase of $\pi/4$. This phase relationship is more consistent with convection (Vescio and Johnson 1992) than gravity waves, where pressure and wind are in phase (Koch and Golus 1988). While ducted gravity waves may have contributed to convective pressure perturbations (Coleman and Knupp 2009), an analysis to confirm such events was precluded by the poor absolute accuracy of MADIS wind observations and the repeated spatial and temporal averaging of wind data by kriging and compositing analysis.

Unlike surface wind perturbations, which are dynamically generated in response to perturbations in pressure, surface temperature perturbations are linked to thermodynamic processes aloft. Consequently, the phase relationship between

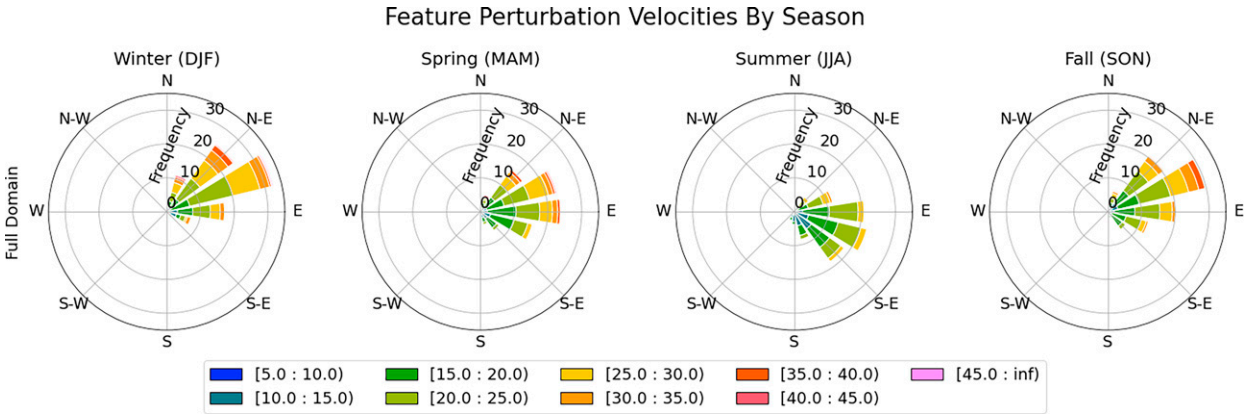

FIG. 14. Stacked histograms of feature velocity by season. Plotted in a polar coordinate system, stacked histograms show the frequency distribution of perturbation speed (r) and direction of propagation (θ). Colors depict bins of different perturbation speeds.

temperature and pressure perturbations was more variable (Fig. 19b), with phases ranging from $\pi/2$ to π. For positive pressure features, temperature perturbations were, on average, approximately $3\pi/2$ out of phase with pressure perturbations of the same sign. For negative pressure features the average phase between temperature and pressure perturbations was slightly more negative (Fig. 19e). This may be explained by the fact that feature-normal winds associated with negative pressure perturbations were marginally weaker than those associated with positive pressure perturbations (Fig. 18b). The phase relationship between pressure and dewpoint perturbations largely mirrored that between pressure and temperature. One exception was that dewpoint perturbations were more frequently in negative phase with pressure perturbations. For 40% of pressure features, dewpoint perturbations lagged pressure perturbations of the same sign. In contrast, only 23% of pressure features exhibited temperature perturbations which lagged pressure perturbations.

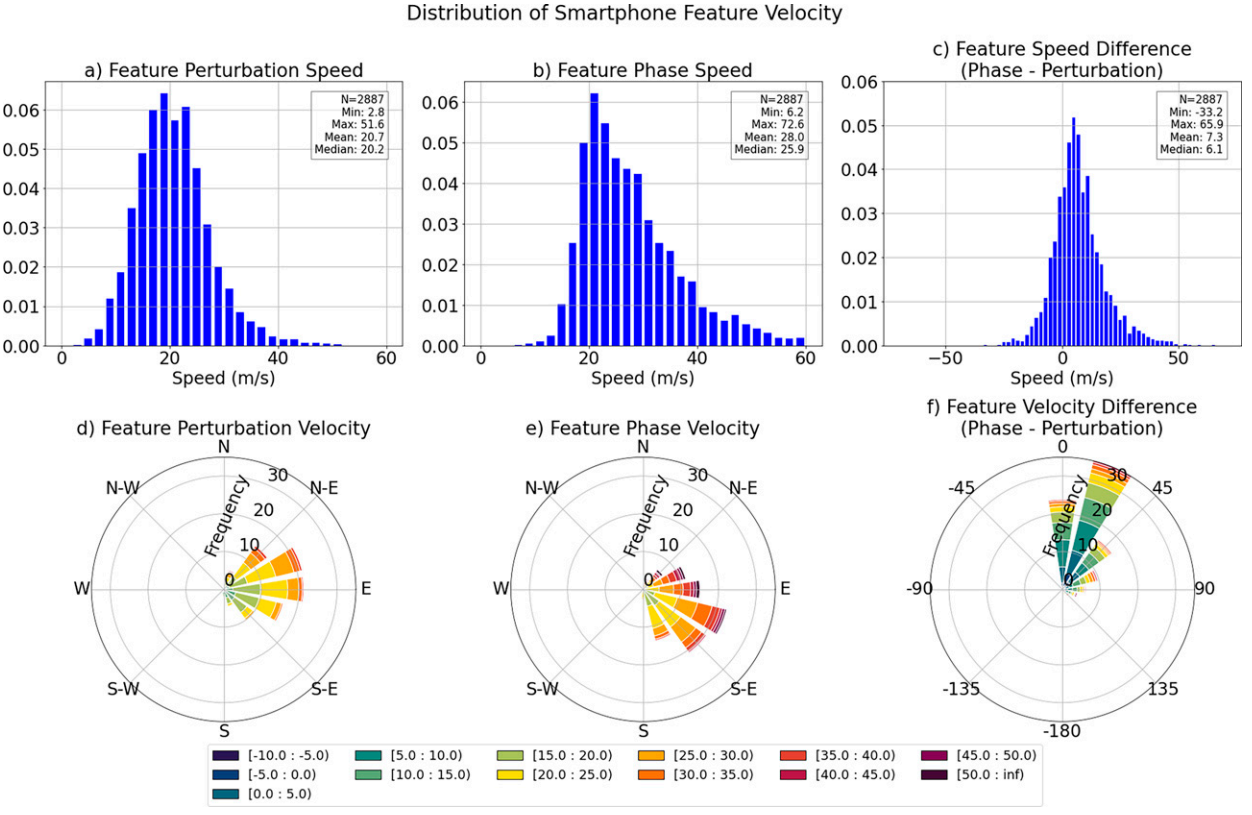

FIG. 15. Distribution of feature speed for (a) feature perturbation speed and (b) phase speed. (c) The difference between phase and perturbation speed is shown. 2D stacked histograms of (d) feature perturbation velocity, (e) phase velocity, and (f) their difference.

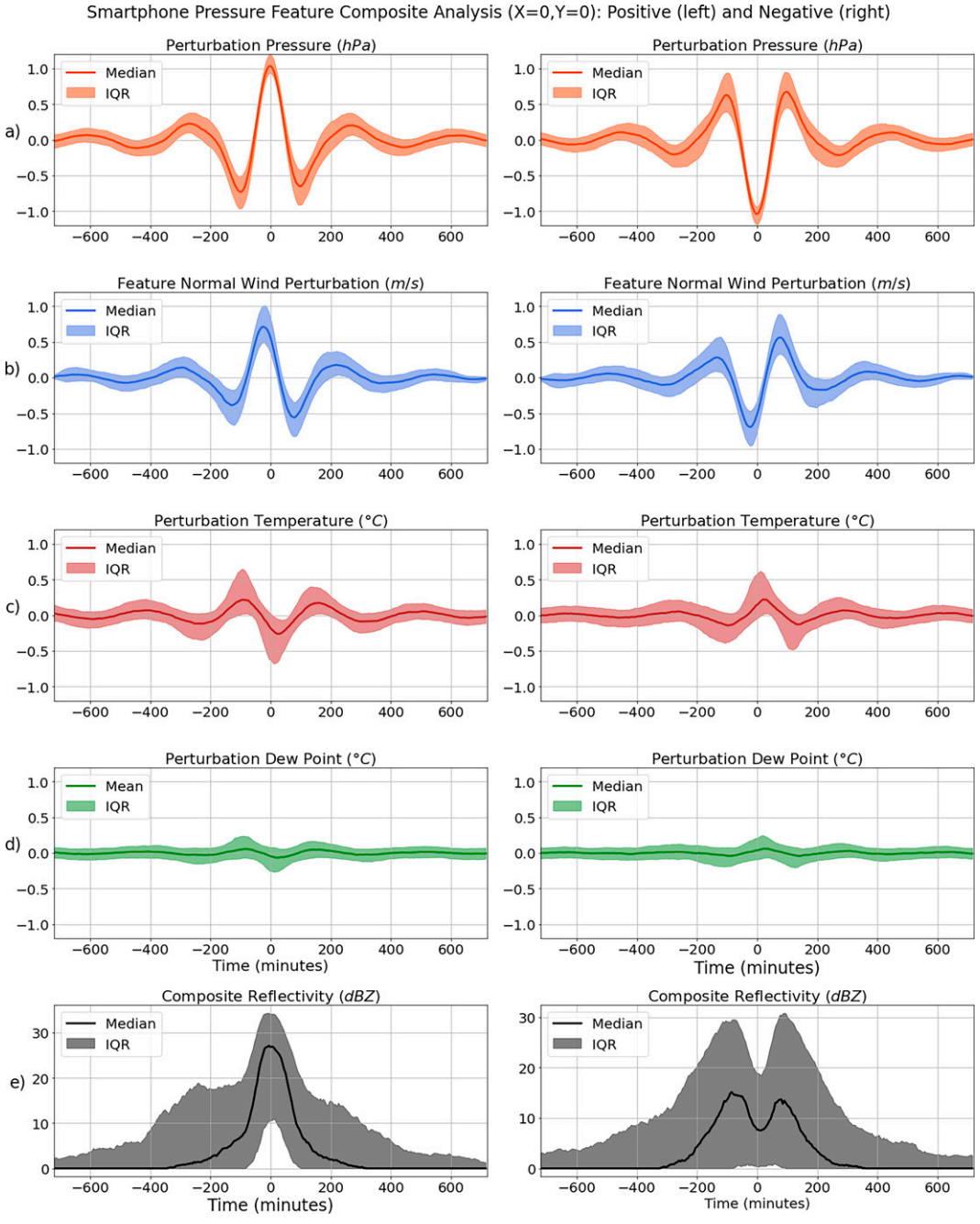

FIG. 16. Distribution of composite time series of (a) perturbation pressure, (b) feature normal wind, (c) temperature, (d) dewpoint, and (e) composite reflectivity for (left) positive and (right) negative smartphone pressure features. Composite time series were retrieved from the center of the composite domain when the pressure feature was centered within the domain.

5. Conclusions

A climatology of mesoscale pressure features was developed to evaluate whether smartphone pressures observations (SPOs) can better resolve mesoscale phenomena than existing surface pressure networks such as MADIS. To produce this climatology, bandpass filtering of smartphone and MADIS surface pressure analyses was performed to extract mesoscale pressure perturbations. To examine how pressure covaries with other parameters, the multiresolution kriging approach from McNicholas and Mass (2021) was adapted to generate MADIS surface analyses of temperature, dewpoint temperature, and wind. Pressure features that lasted at least 1 h, possessed an area

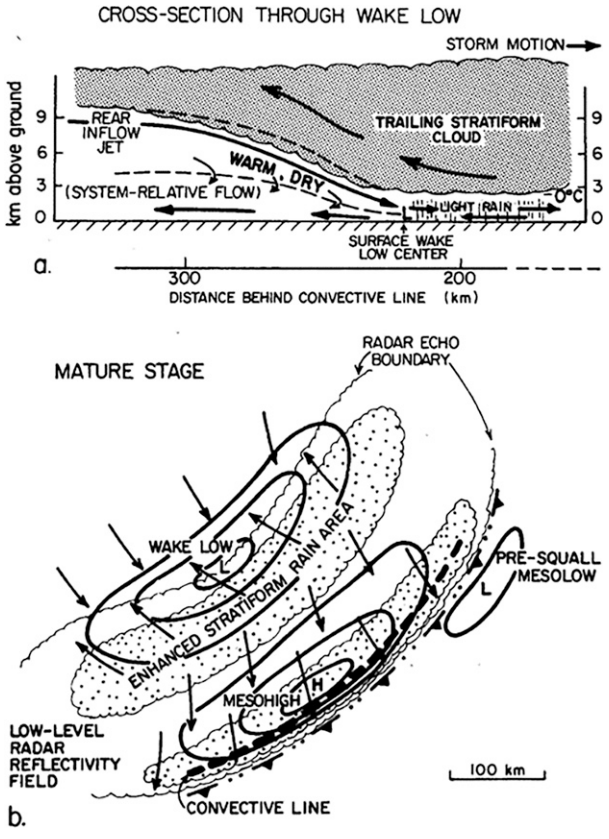

FIG. 17. Schematic cross section through (a) wake low and (b) surface pressure and wind fields and precipitation distribution during squall-line mature stage. [Adapted from Johnson and Hamilton (1988). Copyright American Meteorological Society. Used with permission.]

of at least 2500 km^2, and reached peak absolute amplitude of at least 1 hPa, were tracked to provide a climatology of pressure feature trajectories.

To examine the structure of pressure features and covariate parameters (e.g., wind), a compositing method was developed. In this technique, time series at grid points were retrieved from a 250 km × 250 km bounding box that followed the pressure feature centroid over its lifetime. The resulting ensemble of time series was averaged along the feature track to retrieve the spatial and temporal average evolution of the pressure feature. This methodology of feature tracking and compositing was demonstrated for the case of a squall line.

During 2018, nearly 3000 pressure features were tracked across the central and eastern United States. Almost all (~97%) were in proximity to precipitation at some point during their lifetime, with over five in six associated with convection. Across the analysis domain, smartphone-revealed pressure features outnumbered MADIS pressure features. This was most apparent in the northern and western half of the domain. It appears that the greater number of smartphone pressure features than MADIS-observed features is a consequence of SPOs better-resolving pressure perturbations than MADIS. This result is primarily attributed to the more extensive coverage and higher density of SPOs compared to the sparser conventional observation platforms, particularly in the northwest portion of the domain.

MADIS and smartphone feature counts varied considerably over the year. For both climatologies, the highest feature counts were observed between April and June, with the lowest counts during the fall in September and October. The difference in smartphone and MADIS feature counts peaked in the summer, when synoptic and subsynoptic forcing was weakest. During the spring and summer, local maxima in perturbation events were observed across the Great Plains. Analysis of pressure feature characteristics revealed that, on average, smartphone pressure features traveled 25 km further and lasted 25 min longer than MADIS pressure features. More large-amplitude (>1.5 hPa) pressure perturbations were detected by smartphones (35%) than MADIS (26%).

An examination of smartphone pressure features tracks found that most pressure features propagated eastward. While the centroid of smartphone pressure perturbations propagated at an average speed of 21 m s^{-1} the phase velocity of pressure features, estimated through beamsteering, averaged 28 m s^{-1}. For smartphone pressure features the direction of phase propagation veered from the direction of perturbation propagation.

The composite feature analyses showed regions of divergence and convergence displaced rearward of positive (negative) pressure features that were generally associated with precipitation. In general, positive pressure features were associated with more intense precipitation than negative pressure features, especially during the spring and summer. Spatial composite feature analyses demonstrated that smartphone positive and negative pressure features were consistent with mesohighs and wake low. A local maximum in composite reflectivity lagged convergence behind the negative pressure perturbation suggesting some pressure features may have contributed to incipient convection to the rear of the pressure wave.

Composite feature analyses were used to derive quantitative estimates of the coherence and phase of pressure perturbations with respect to temperature, dewpoint, and feature normal wind perturbations. The results showed that the coherence of pressure and feature-normal wind perturbations was greater than the coherence of pressure and temperature perturbations. For most pressure features, the feature normal wind perturbations lead pressure perturbations by a phase of $\pi/4$.

Overall, analysis of smartphone and MADIS pressure climatology revealed that bias-corrected SPOs can capture mesoscale pressure features poorly observed by existing pressure networks, like MADIS, in regions where observation density is sparse. The climatology of surface pressure features largely reflected the geographic, seasonal, and diurnal variation of organized mesoscale convection. Feature characteristics such as propagation velocity, duration, and distance traveled were consistent with prior analysis of mesoscale pressure perturbations by Jacques et al. (2017). Phase relationships between mesoscale pressure perturbations and other surface state variables were consistent with those expected for mesohighs and wake lows associated with convection.

This work demonstrates that smartphone observations can supplement existing surface pressure networks, especially for mesoscale pressure features. By better resolving mesoscale

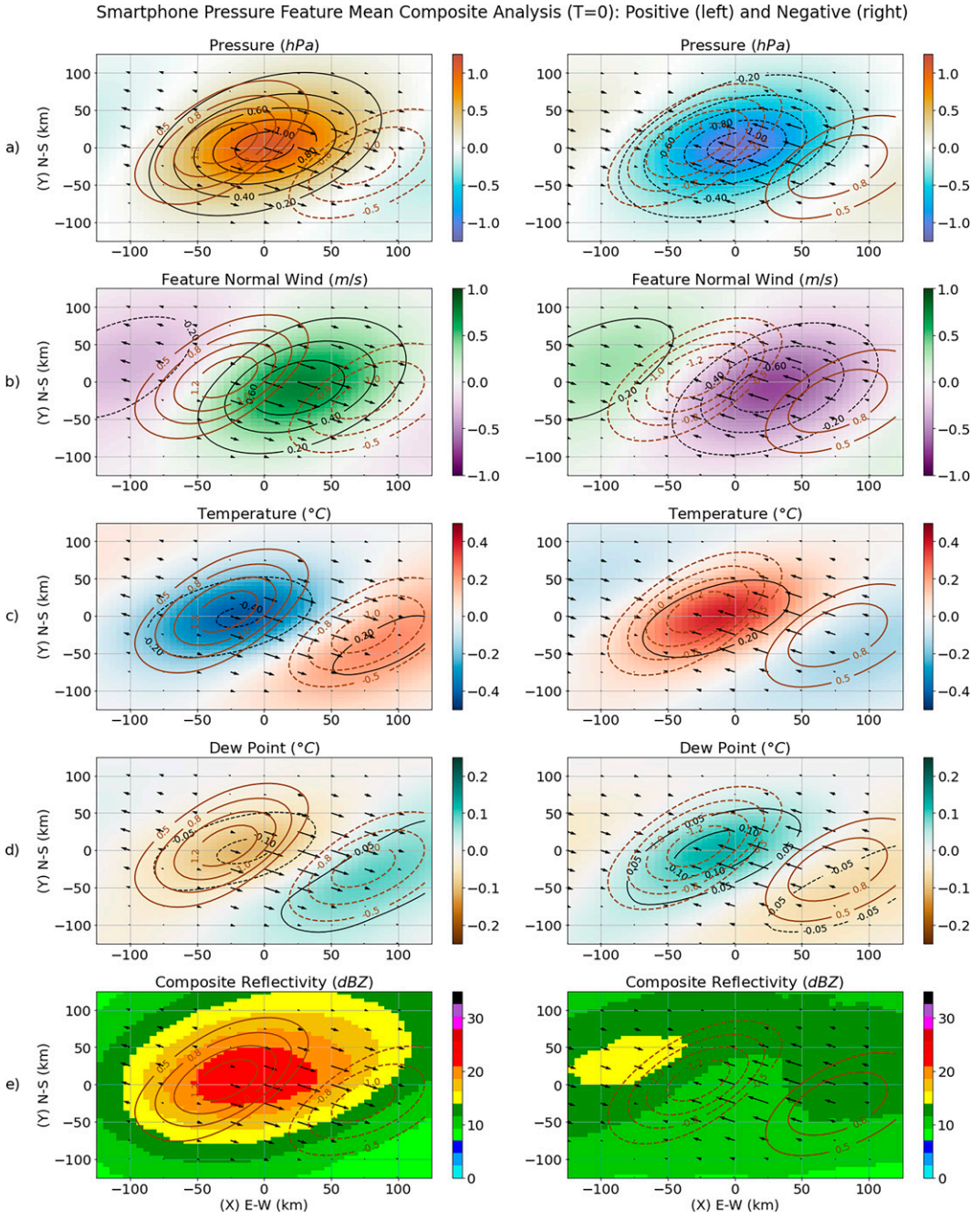

FIG. 18. Average composite analyses of (a) perturbation pressure, (b) feature normal wind, (c) temperature, (d) dewpoint temperature, and (e) composite reflectivity for (left) positive and (right) negative smartphone pressure features. Spatial averaging of composites was performed at the center of the compositing time window ($T = 0$) when the pressure feature was centered within the composite domain. Brown contours depict regions of divergence (solid) and convergence (dashed) in units of 10^{-5} s^{-1}.

structures and features, such as wake lows and mesohighs, smartphones have the potential to enhance the analysis and forecasting of convection.

Acknowledgments. The authors acknowledge IBM (The Weather Company) for their financial support of this research and their provision of pressure data. Peter Neilley of the Weather Company was instrumental in the acquisition of IBM smartphone pressure data.

Data availability statement. Conventional surface pressure observations from ASOS stations were retrieved from the

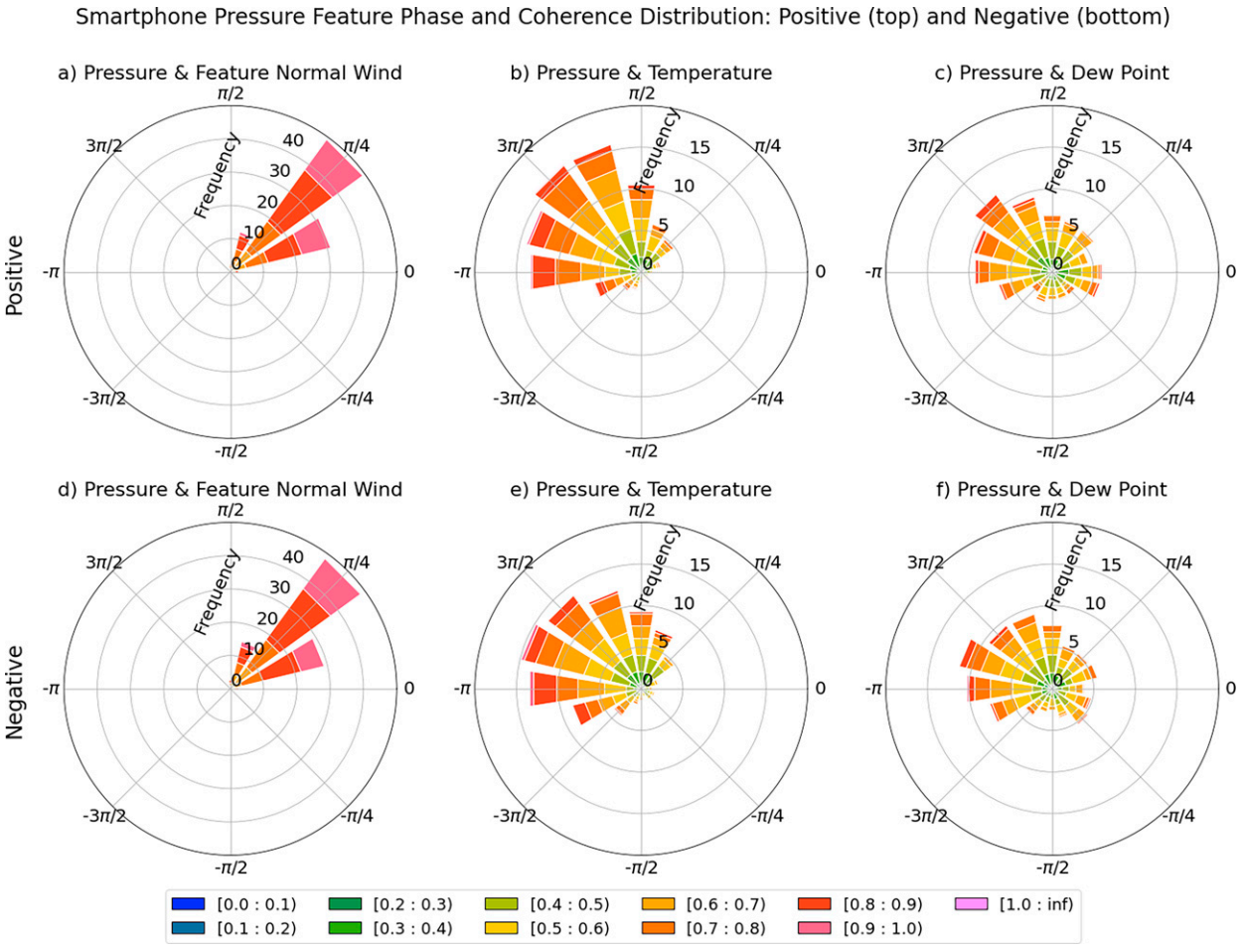

FIG. 19. 2D stacked histograms of phase and coherence between perturbation pressure and feature (a),(d) normal perturbation wind; (b),(e) perturbation temperature; and (c),(f) perturbation dewpoint temperature for (top) positive and (bottom) negative smartphone pressure features. Stacked histograms show the frequency distribution of coherence (r) and phase (θ).

National Climatic Data Center (NCEI 2018) for the following website: https://www.ncdc.noaa.gov/data-access/land-based–station-data/land-based-datasets/automated-surface-observing-system-asos. METAR and meteorological surface (i.e., Mesonet) observations from MADIS are available through a request from https://madis.ncep.noaa.gov/data_application.shtml. In this study, surface pressure observations from restricted Mesonets were used. These observations are not publicly accessible and are only available to researchers (https://madis.ncep.noaa.gov/madis_restrictions.shtml). Due to privacy and ethical concerns, as well as confidentiality agreements and data storage limitations, the smartphone pressure observations used in this study cannot be made publicly available. The source code used to generate all figures in this paper is provided in the open-source repository meteo-krig (https://github.com/cmac994/meteo-krig). In this repository, the generation of smartphone pressure and MADIS surface analysis is demonstrated. Furthermore, the identification, tracking, and compositing of mesoscale pressure features is illustrated through the case study of a squall line. Linked with this repository is an archive containing all data used to produce the figures in this article. These data include but are not limited to surface analysis, mesoscale perturbation analyses, smartphone and MADIS feature tracks/statistics, and composite feature analysis.

APPENDIX

Beamsteering Analysis

While lag analysis has been used in the past to extract wave parameters from surface pressure perturbations (Rees and Mobbs 1988), beamsteering has also been applied to determine horizontal wave speeds and directions from surface pressure variations (Einaudi et al. 1989; Hauf et al. 1996; Denholm-Price and Rees 1998; Rees et al. 2000; de Groot Hedlin et al. 2017). One advantage of beamsteering, over lag analysis, is that it is accurate across a range of frequencies and wave parameters (Rees et al. 2000). In beamsteering, a "beam" is steered in the frequency domain until a horizontal wave vector and wave

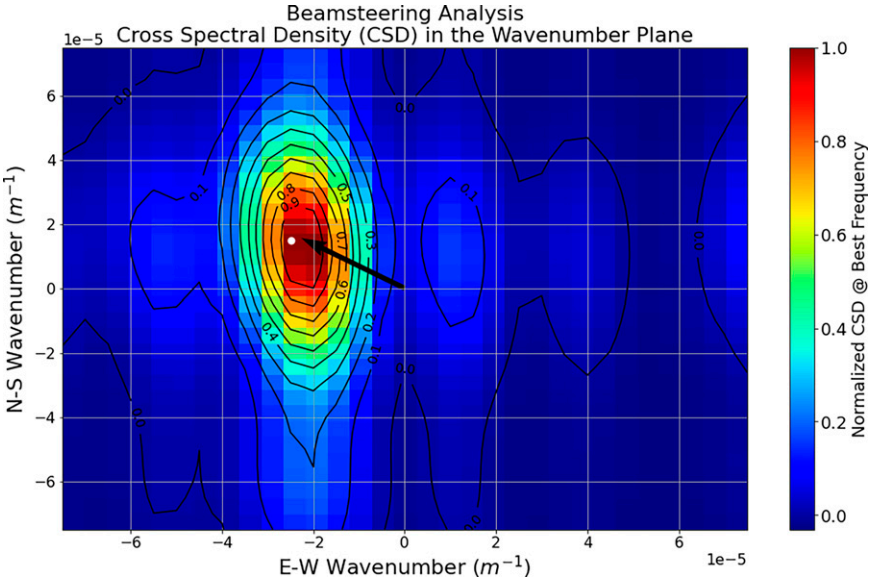

FIG. A1. Beamsteering analysis in the frequency/wavenumber domain. The arrow *beam* points to the location of max cross-power spectral density (white dot) in the wavenumber domain. The direction of the beam indicates the direction from which the feature was propagating.

frequency is found which maximizes the cross-power spectral density between all pairs of station pairs. In composite feature analysis (Fig. 4), station pairs are taken as grid points along the composite feature track. Mathematically, beamsteering in the frequency domain is performed by calculating the array power spectrum, which is the sum of the cross-spectral power density over all combinations of grid point pairs (Nappo 2012):

$$\hat{G}(\omega, \mathbf{k}) = \sum_{i=1}^{M} \sum_{j=1}^{M} G_{ij}(\omega) \exp(i\mathbf{k} \cdot \mathbf{d}_{ij}). \tag{A1}$$

In practice, Eq. (1) is calculated by searching across the frequency and wavenumber domain for the values of ω and $\mathbf{k}$ which maximize the array power spectrum $\hat{G}$. Once found, ω and $\mathbf{k}$ can be used to calculate the slowness components: $S_x = k/\omega$, $S_y = l/\omega$. In beamsteering the slowness vector $\mathbf{S}$ is defined as follows:

$$\mathbf{S} = \left(\frac{1}{c_x}\right)\hat{\mathbf{x}} + \left(\frac{1}{c_y}\right)\hat{\mathbf{y}}, \tag{A2}$$

with components S_x and S_y (Nappo 2012). The slowness vector has a magnitude of $1/c$ and is always parallel to the direction of propagation of the feature. After retrieving slowness components, an estimate of the feature speed c and direction of propagation (phase) can be calculated:

$$c = \frac{1}{\sqrt{S_x^2 + S_y^2}}, \tag{A3}$$

$$\phi = \tan^{-1}\left(\frac{S_x}{S_y}\right). \tag{A4}$$

Beamsteering analysis in the frequency domain was applied to the pressure feature examined in Fig. 4. The result is displayed in Fig. A1, which shows the distribution of normalized cross-power spectral density (CSD), plotted as a function of wavenumber for the angular frequency ω at which the peak CSD was found. The black arrow in the figure represents the "beam" and points to the peak in the CSD in the wavenumber domain. Note that in Fig. A1 the angle of the beam, with respect to the abscissa, represents the direction *from* which the feature is propagating.

REFERENCES

Adams-Selin, R. D., and R. H. Johnson, 2010: Mesoscale surface pressure and temperature features associated with bow echoes. *Mon. Wea. Rev.*, **138**, 212–227, https://doi.org/10.1175/2009MWR2892.1.

——, and ——, 2013: Examination of gravity waves associated with the 13 March 2003 bow echo. *Mon. Wea. Rev.*, **141**, 3735–3756, https://doi.org/10.1175/MWR-D-12-00343.1.

Alexander, C., and Coauthors, 2017: WRF-ARW research to operations update: The Rapid-Refresh (RAP) version 4, High-Resolution Rapid Refresh (HRRR) version 3 and convection-allowing ensemble prediction. *18th WRF User's Workshop*, UCAR–NCAR, Boulder, CO, 2.5, https://ruc.noaa.gov/ruc/ppt_pres/Alexander_WRFworkshop_2017_Final.pdf.

Allan, D., T. A. Caswell, N. Keim, F. Boulogne, R. W. Perry, and L. Uieda, 2014: soft-matter/trackpy: Trackpy v0.4.2. Zenodo, accessed 15 July 2021, https://doi.org/10.5281/zenodo.3492186.

Blaylock, B., J. Horel, and S. Liston, 2017: Cloud archiving and data mining of High-Resolution Rapid Refresh forecast model output. *Comput. Geosci.*, **109**, 43–50, https://doi.org/10.1016/j.cageo.2017.08.005.

Chen, T., and C. Guestrin, 2016: XGBoost: A scalable tree boosting system. *Proc. 22nd ACM SIGKDD Int. Conf. on Knowledge Discovery and Data Mining (KDD'16)*, San Francisco, CA, Association for Computing Machinery, 785–794, https://doi.org/10.1145/2939672.2939785.

COESA, 1976: *U.S. Standard Atmosphere, 1976.* NOAA, 227 pp.

Coleman, T. A., and K. R. Knupp, 2009: Factors affecting surface wind speeds in gravity waves and wake lows. *Wea. Forecasting*, **24**, 1664–1679, https://doi.org/10.1175/2009WAF2222248.1.

Crawford, T. M., and H. B. Bluestein, 1997: Characteristics of dryline passage during COPS-91. *Mon. Wea. Rev.*, **125**, 463–477, https://doi.org/10.1175/1520-0493(1997)125<0463:CODPDC>2.0.CO;2.

de Groot-Hedlin, C. D., M. A. H. Hedlin, L. Hoffmann, M. J. Alexander, and C. C. Stephan, 2017: Relationships between gravity waves observed at Earth's surface and in the stratosphere over the central and eastern United States. *J. Geophys. Res. Atmos.*, **122**, 11 482–11 498, https://doi.org/10.1002/2017JD027159.

Denholm-Price, J. C. W., and J. M. Rees, 1998: A practical example of low-frequency trend removal. *Bound.-Layer Meteor.*, **86**, 181–187, https://doi.org/10.1023/A:1000566921106.

de Pondeca, M., and Coauthors, 2011: The real-time mesoscale analysis at NOAA's National Centers for Environmental Prediction: Current status and development. *Wea. Forecasting*, **26**, 593–612, https://doi.org/10.1175/WAF-D-10-05037.1.

Einaudi, F., A. J. Bedard, and J. J. Finnigan, 1989: A climatology of gravity waves and other coherent disturbances at the Boulder Atmospheric Observatory during March–April 1984. *J. Atmos. Sci.*, **46**, 303–329, https://doi.org/10.1175/1520-0469(1989)046<0303:ACOGWA>2.0.CO;2.

Engerer, N. A., D. J. Stensrud, and M. C. Coniglio, 2008: Surface characteristics of observed cold pools. *Mon. Wea. Rev.*, **136**, 4839–4849, https://doi.org/10.1175/2008MWR2528.1.

Ester, M., H.-P. Kriegel, J. Sander, and X. Xu, 1996: A density-based algorithm for discovering clusters in large spatial databases with noise. *KDD'96: Proceedings of the Second International Conference on Knowledge Discovery and Data Mining*, E. Simoudis, J. Han, and U. Fayyad, Eds., AAAI Press, 226–231, https://www.aaai.org/Papers/KDD/1996/KDD96-037.pdf.

Evans, J. S., and C. A. Doswell III, 2001: Examination of derecho environments using proximity soundings. *Wea. Forecasting*, **16**, 329–342, https://doi.org/10.1175/1520-0434(2001)016<0329:EODEUP>2.0.CO;2.

Fritts, D. C., and M. J. Alexander, 2003: Gravity wave dynamics and effects in the middle atmosphere. *Rev. Geophys.*, **41**, 1003, https://doi.org/10.1029/2001RG000106.

Fujita, T. T., 1955: Results of detailed synoptic studies of squall lines. *Tellus*, **7**, 405–436, https://doi.org/10.3402/tellusa.v7i4.8920.

Gaberšek, S., and D. R. Durran, 2006: Gap flows through idealized topography. Part II: Effects of rotation and surface friction. *J. Atmos. Sci.*, **63**, 2720–2739, https://doi.org/10.1175/JAS3786.1.

Geerts, B., Q. Miao, and J. C. Demko, 2008: Pressure perturbations and upslope flow over a heated, isolated mountain. *Mon. Wea. Rev.*, **136**, 4272–4288, https://doi.org/10.1175/2008MWR2546.1.

Giovannini, L., L. Laiti, S. Serafin, and D. Zardi, 2017: The thermally driven diurnal wind system of the Adige Valley in the Italian Alps. *Quart. J. Roy. Meteor. Soc.*, **143**, 2389–2402, https://doi.org/10.1002/qj.3092.

Haberlie, A. M., and W. S. Ashley, 2019: A radar-based climatology of mesoscale convective systems in the United States. *J. Climate*, **32**, 1591–1606, https://doi.org/10.1175/JCLI-D-18-0559.1.

Haertel, P. T., and R. H. Johnson, 2000: The linear dynamics of squall line mesohighs and wake lows. *J. Atmos. Sci.*, **57**, 93–107, https://doi.org/10.1175/1520-0469(2000)057<0093:TLDOSL>2.0.CO;2.

Hauf, T., U. Finke, J. Neisser, G. Bull, and J.-G. Stangenberg, 1996: A ground-based network for atmospheric pressure fluctuations. *J. Atmos. Oceanic Technol.*, **13**, 1001–1023, https://doi.org/10.1175/1520-0426(1996)013<1001:AGBNFA>2.0.CO;2.

Hooke, W. H., and R. M. Jones, 1986: Dissipative waves excited by gravity-wave encounters with the stably stratified planetary boundary layer. *J. Atmos. Sci.*, **43**, 2048–2060, https://doi.org/10.1175/1520-0469(1986)043<2048:DWEBGW>2.0.CO;2.

Jacques, A. A., J. D. Horel, E. T. Crosman, and F. L. Vernon, 2015: Central and eastern U.S. surface pressure variations derived from the USArray network. *Mon. Wea. Rev.*, **143**, 1472–1493, https://doi.org/10.1175/MWR-D-14-00274.1.

——, ——, ——, and ——, 2017: Tracking mesoscale pressure perturbations using the USArray transportable array. *Mon. Wea. Rev.*, **145**, 3119–3142, https://doi.org/10.1175/MWR-D-16-0450.1.

Jewett, B. F., M. K. Ramamurthy, and R. M. Rauber, 2003: Origin, evolution, and finescale structure of the St. Valentine's Day mesoscale gravity wave observed during STORM-FEST. Part III: Gravity wave genesis and the role of evaporation. *Mon. Wea. Rev.*, **131**, 617–633, https://doi.org/10.1175/1520-0493(2003)131<0617:OEAFSO>2.0.CO;2.

Johnson, R. H., and P. J. Hamilton, 1988: The relationship of surface pressure features to the precipitation and airflow structure of an intense midlatitude squall line. *Mon. Wea. Rev.*, **116**, 1444–1473, https://doi.org/10.1175/1520-0493(1988)116<1444:TROSPF>2.0.CO;2.

Kim, Y.-J., S. D. Eckermann, and H.-Y. Chun, 2003: An overview of the past, present, and future of gravity-wave drag parameterization for numerical climate and weather prediction models. *Atmos.–Ocean*, **41**, 65–98, https://doi.org/10.3137/ao.410105.

Koch, S. E., and R. E. Golus, 1988: A mesoscale gravity wave event observed during CCOPE. Part I: Multiscale statistical analysis of wave characteristics. *Mon. Wea. Rev.*, **116**, 2527–2544, https://doi.org/10.1175/1520-0493(1988)116<2527:AMGWEO>2.0.CO;2.

——, and C. O'Handley, 1997: Operational forecasting and detection of mesoscale gravity waves. *Wea. Forecasting*, **12**, 253–281, https://doi.org/10.1175/1520-0434(1997)012<0253:OFADOM>2.0.CO;2.

——, and S. Saleeby, 2001: An automated system for the analysis of gravity waves and other mesoscale phenomena. *Wea. Forecasting*, **16**, 661–679, https://doi.org/10.1175/1520-0434(2001)016<0661:AASFTA>2.0.CO;2.

Koppel, L. L., L. F. Bosart, and D. Keyser, 2000: A 25-yr climatology of large-amplitude hourly surface pressure changes over the conterminous United States. *Mon. Wea. Rev.*, **128**, 51–68, https://doi.org/10.1175/1520-0493(2000)128<0051:AYCOLA>2.0.CO;2.

Li, Y., and R. B. Smith, 2010: The detection and significance of diurnal pressure and potential vorticity anomalies east of the Rockies. *J. Atmos. Sci.*, **67**, 2734–2751, https://doi.org/10.1175/2010JAS3423.1.

——, ——, and V. Grubišić, 2009: Using surface pressure variations to categorize diurnal valley circulations: Experiments in

Owens Valley. *Mon. Wea. Rev.*, **137**, 1753–1769, https://doi.org/10.1175/2008MWR2495.1.

Madaus, L. E., and C. F. Mass, 2017: Evaluating smartphone pressure observations for mesoscale analyses and forecasts. *Wea. Forecasting*, **32**, 511–531, https://doi.org/10.1175/WAF-D-16-0135.1.

——, G. J. Hakim, and C. F. Mass, 2014: Utility of dense pressure observations for improving mesoscale analyses and forecasts. *Mon. Wea. Rev.*, **142**, 2398–2413, https://doi.org/10.1175/MWR-D-13-00269.1.

MADIS, 2017: MADIS meteorological surface quality control checks. Accessed 4 March 2021, https://madis.ncep.noaa.gov/madis_sfc_qc_notes.shtml.

Mandement M., and O. Caumont, 2020: Contribution of personal weather stations to the observation of deep-convection features near the ground. *Nat. Hazards Earth Syst. Sci.*, **20**, 299–322, https://doi.org/10.5194/nhess-20-299-2020.

Mass, C. F., W. J. Steenburgh, and D. M. Schultz, 1991: Diurnal surface-pressure variations over the continental United States and the influence of sea-level reduction. *Mon. Wea. Rev.*, **119**, 2814–2830, https://doi.org/10.1175/1520-0493(1991)119<2814:DSPVOT>2.0.CO;2.

McNicholas, C., and C. Mass, 2018: Smartphone pressure collection and bias correction using machine learning. *J. Atmos. Oceanic Technol.*, **35**, 523–540, https://doi.org/10.1175/JTECH-D-17-0096.1.

——, and ——, 2021: Bias correction, anonymization, and analysis of smartphone pressure observations using machine learning and multi-resolution kriging. *Wea. Forecasting*, **36**, 1867–1889, https://doi.org/10.1175/WAF-D-20-0222.1.

Metz, N. D., and L. F. Bosart, 2010: Derecho and MCS development, evolution, and multiscale interactions during 3–5 July 2003. *Mon. Wea. Rev.*, **138**, 3048–3070, https://doi.org/10.1175/2010MWR3218.1.

Miller, P. A., and S. G. Benjamin, 1992: A system for the hourly assimilation of surface observations in mountainous and flat terrain. *Mon. Wea. Rev.*, **120**, 2342–2359, https://doi.org/10.1175/1520-0493(1992)120<2342:ASFTHA>2.0.CO;2.

——, M. F. Barth, and L. A. Benjamin, 2005: An update on MADIS observation ingest, integration, quality control, and distribution capabilities. *21st Int. Conf. on Interactive Information and Processing Systems (IIPS) for Meteorology, Oceanography, and Hydrology,* San Diego, CA, Amer. Meteor. Soc., J7.12, https://ams.confex.com/ams/Annual2005/techprogram/paper_86703.htm.

Nappo, C. J., 2012: *An Introduction to Atmospheric Gravity Waves.* 2nd ed. Elsevier Science & Technology, 279 pp.

NCEI, 2018: 1-minute Automated Surface Observing System (ASOS) data. NOAA, accessed 23 November 2020, https://www.ncei.noaa.gov/products/land-based-station/automated-surface-weather-observing-systems.

Novak, D. R., and B. A. Colle, 2006: Observations of multiple sea breeze boundaries during an unseasonably warm day in metropolitan New York City. *Bull. Amer. Meteor. Soc.*, **87**, 169–174, https://doi.org/10.1175/BAMS-87-2-169.

Nychka, D., S. Bandyopadhyay, D. Hammerling, F. Lindgren, and S. Sain, 2015: A multiresolution Gaussian process model for the analysis of large spatial datasets. *J. Comput. Graph. Stat.*, **24**, 579–599, https://doi.org/10.1080/10618600.2014.914946.

——, D. Hammerling, S. Sain, and N. Lenssen, 2016: LatticeKrig: Multiresolution kriging based on Markov random fields. R package version 8.4, accessed 1 June 2020, https://doi.org/10.5065/D6HD7T1R.

Pedatella, N. M., H.-L. Liu, and A. D. Richmond, 2012: Atmospheric semidiurnal lunar tide climatology simulated by the Whole Atmosphere Community Climate Model. *J. Geophys. Res.*, **117**, A06327, https://doi.org/10.1029/2012JA017792.

Price, C., R. Maor, and H. Shachaf, 2018: Using smartphones for monitoring atmospheric tides. *J. Atmos. Sol.-Terr. Phys.*, **174**, 1–4, https://doi.org/10.1016/j.jastp.2018.04.015.

Rees, J. M., and S. D. Mobbs, 1988: Studies of internal gravity waves at Halley Station, Antarctica, using wind observations. *Quart. J. Roy. Meteor. Soc.*, **114**, 939–966, https://doi.org/10.1002/qj.49711448206.

——, J. C. W. Denholm-Price, J. C. King, and P. S. Anderson, 2000: A climatological study of internal gravity waves in the atmospheric boundary layer overlying the Brunt Ice Shelf, Antarctica. *J. Atmos. Sci.*, **57**, 511–526, https://doi.org/10.1175/1520-0469(2000)057<0511:ACSOIG>2.0.CO;2.

Tyndall, D. P., and J. D. Horel, 2013: Impacts of mesonet observations on meteorological surface analyses. *Wea. Forecasting*, **28**, 254–269, https://doi.org/10.1175/WAF-D-12-00027.1.

Tytell, J., F. Vernon, M. Hedlin, C. de Groot Hedlin, J. Reyes, B. Busby, K. Hafner, and J. Eakins, 2016: The USArray Transportable Array as a platform for weather observation and research. *Bull. Amer. Meteor. Soc.*, **97**, 603–619, https://doi.org/10.1175/BAMS-D-14-00204.1.

Vescio, M. D., and R. H. Johnson, 1992: The surface-wind response to transient mesoscale pressure fields associated with squall lines. *Mon. Wea. Rev.*, **120**, 1837–1850, https://doi.org/10.1175/1520-0493(1992)120<1837:TSWRTT>2.0.CO;2.

Viana, S., E. Terradellas, and C. Yagüe, 2010: Analysis of gravity waves generated at the top of a drainage flow. *J. Atmos. Sci.*, **67**, 3949–3966, https://doi.org/10.1175/2010JAS3508.1.